

2

NAVY
NAVAL POSTGRADUATE SCHOOL
Monterey, California

AD-A219 541



THESIS

DEC 1990
D

KINEMATICS UNDER WIND WAVES

by

Manuel P. Abreu

September 1989

Thesis Advisor
Co-Advisor

Edward B. Thornton
T. P. Stanton

Approved for public release; distribution is unlimited.

90 03 28 000

Unclassified

security classification of this page

REPORT DOCUMENTATION PAGE				
1a Report Security Classification Unclassified			1b Restrictive Markings	
2a Security Classification Authority			3 Distribution Availability of Report Approved for public release; distribution is unlimited.	
2b Declassification Downgrading Schedule				
4 Performing Organization Report Number(s)			5 Monitoring Organization Report Number(s)	
6a Name of Performing Organization Naval Postgraduate School	6b Office Symbol (if applicable) 35		7a Name of Monitoring Organization Naval Postgraduate School	
6c Address (city, state, and ZIP code) Monterey, CA 93943-5000			7b Address (city, state, and ZIP code) Monterey, CA 93943-5000	
8a Name of Funding Sponsoring Organization	8b Office Symbol (if applicable)		9 Procurement Instrument Identification Number	
8c Address (city, state, and ZIP code)			10 Source of Funding Numbers	
			Program Element No	Project No
			Task No	Work Unit Accession No
11 Title (include security classification) KINEMATICS UNDER WIND WAVES (Unclassified)				
12 Personal Author(s) Manuel P. Abreu				
13a Type of Report Master's Thesis		13b Time Covered From To		14 Date of Report (year, month, day) September 1989
				15 Page Count 82
16 Supplementary Notation The views expressed in this thesis are those of the author and do not reflect the official policy or position of the Department of Defense or the U.S. Government.				
17 Cosati Codes			18 Subject Terms (continue on reverse if necessary and identify by block number)	
Field	Group	Subgroup	Wind Waves, Kinematics, <i>REPORT 0012, Thesis 1471, PACIFIC OCEAN</i>	
			<i>SA-001</i>	
19 Abstract (continue on reverse if necessary and identify by block number)				
<p>The ocean near surface kinematics were measured as part of the SAXON experiment during the period from 5 to 14 October 1988. A growing wave field due to a passing front with winds up to 17 ms^{-1} occurred during the first 5 days. A wide range of wind forcing and wave conditions occurred during the measurement period. Two orthogonal components of the horizontal velocity were measured using an electromagnetic current meter. The wave directional field was measured using a high resolution 2 meter square slope array. The classical Longuet-Higgins et al (1963) method of computing directional wave spectra and the new exact Fourier coefficients representation method (Grauzinis, 1989) are used to compute directional wave spectra. The new method of computing directional wave spectra, which represents bi-modal distributions of wave energy exactly matching the measured Fourier coefficients to second order, demonstrated improved performance over the classical technique. Phase functions between the sea surface elevation and horizontal velocity components compared well with the results predicted by linear wave theory. The coherence function of the horizontal velocity components and the sea surface elevation confirmed the dependence on the wave field directivity. Spectra of the sea surface elevation computed from pressure and horizontal velocity data compared well using linear theory transfer functions.</p>				
20 Distribution Availability of Abstract			21 Abstract Security Classification	
<input checked="" type="checkbox"/> unclassified unlimited <input type="checkbox"/> same as report <input type="checkbox"/> DTIC users			Unclassified	
22a Name of Responsible Individual Edward B. Thornton			22b Telephone (include Area code) (408) 646-2847	22c Office Symbol 6STM

DD FORM 1473.84 MAR

83 APR edition may be used until exhausted
All other editions are obsolete

security classification of this page

Unclassified

Approved for public release; distribution is unlimited.

Kinematics under Wind Waves

by

Manuel P. Abreu
Lieutenant , Portuguese Navy
B.Sc., Portuguese Naval Academy, 1983


Submitted in partial fulfillment of the
requirements for the degree of

MASTER OF SCIENCE IN OCEANOGRAPHY

from the

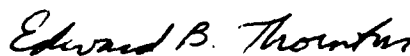
NAVAL POSTGRADUATE SCHOOL
September 1989

Author:



Manuel P. Abreu

Approved by:



Edward B. Thornton, Thesis Advisor



T. P. Stanton, Co-Advisor



Curtis A. Collins, Chairman,
Department of Oceanography

ABSTRACT

The ocean near surface kinematics were measured as part of the SAXON experiment during the period from 5 to 14 October 1988. A growing wave field due to a passing front with winds up to 17 ms^{-1} occurred during the first 5 days. A wide range of wind forcing and wave conditions occurred during the measurement period. Two orthogonal components of the horizontal velocity were measured using an electromagnetic current meter. The wave directional field was measured using a high resolution 2 meter square slope array. The classical Longuet-Higgins et al (1963) method of computing directional wave spectra and the new exact Fourier coefficients representation method (Grauzinis, 1989) are used to compute directional wave spectra. The new method of computing directional wave spectra, which represents bi-modal distributions of wave energy exactly matching the measured Fourier coefficients to second order, demonstrated improved performance over the classical technique. Phase functions between the sea surface elevation and horizontal velocity components compared well with the results predicted by linear wave theory. The coherence function of the horizontal velocity components and the sea surface elevation confirmed the dependence on the wave field directivity. Spectra of the sea surface elevation computed from pressure and horizontal velocity data compared well using linear theory transfer functions.

Accession For	
NTIS 0-221	<input checked="" type="checkbox"/>
DTIC 7	<input checked="" type="checkbox"/>
Un	<input type="checkbox"/>
Sub	<input type="checkbox"/>
By	
Director/	
Approved by	
Date	
Dist	
A-1	



TABLE OF CONTENTS

I. INTRODUCTION	1
A. THE PROBLEM	1
B. THE OBSERVATIONAL EFFORT	1
C. THE OBJECTIVES	2
II. THEORETICAL AND OBSERVATIONAL BACKGROUND	4
A. THE LINEAR WAVE THEORY	4
1. Formulation	4
2. Spectral and statistical relations	6
B. THE SPECIFICATION OF A WAVE FIELD	7
1. Wave field description	8
2. Directional spectrum	10
3. Classical approach	11
4. Exact Fourier coefficient representation method	14
C. THE VELOCITY FIELD	19
1. Means and fluctuations	19
2. The mean velocity field	21
3. The fluctuating field	25
4. Velocity field and surface elevation	26
III. EXPERIMENT	37
A. LOCATION	37
B. INSTRUMENTATION	39
1. Electromagnetic current meter	39
2. Pressure transducers	39
3. Bistatic acoustic doppler profiler (CADVP)	40
C. DATA ACQUISITION SYSTEM	41
D. DATA	42
1. Processing	42
IV. RESULTS	49

A. A FULL PERIOD ANALYSIS	49
1. Wind and Waves.	49
2. Horizontal velocity	51
3. Air and sea temperature	51
B. SELECTED PERIOD ANALYSIS	51
1. P11	53
2. P12	55
3. P13	58
C. DISCUSSION	63
1. Directional wave spectrum	63
2. Coherence function	66
3. Phase spectrum	68
4. The spectrum of the sea surface elevation	68
V. CONCLUSIONS AND RECOMMENDATIONS	69
LIST OF REFERENCES	71
INITIAL DISTRIBUTION LIST	73

LIST OF TABLES

Table 1. RESULTS OF TESTS TO THE GRAUZINIS METHOD OF COMPUTING DIRECTIONAL WAVE SPECTRUM	48
--	----

LIST OF FIGURES

Figure 1.	The Problem	3
Figure 2.	Typical spreading function of the LCS method	14
Figure 3.	Distributions of energy	16
Figure 4.	Three model distributions	18
Figure 5.	Mean drift current profiles after Wu	23
Figure 6.	Mean velocity profile after Churchill and Csanady	24
Figure 7.	Mean velocities in the upper ocean boundary layer after Richman et al.	25
Figure 8.	Coherence function between the sea surface elevation and the vertical component of the fluctuating velocity field after Yefimov and Khristoforov	32
Figure 9.	Coherence function between the sea surface elevation and the vertical component of the fluctuating velocity after Thornton and Kraphol ...	33
Figure 10.	Spectra of the horizontal and vertical fluctuating velocity components after Shonting	34
Figure 11.	Phase function between the horizontal and the vertical fluctuating veloc- ity and the sea surface elevation after Thornton and Kraphol	35
Figure 12.	Phase function between the vertical and horizontal velocity components and the sea surface elevation after Cavaleri and Zecchetto	36
Figure 13.	Location of the Chesapeake Light Tower	38
Figure 14.	The Chesapeake Light Tower	40
Figure 15.	The frame of the instruments	41
Figure 16.	The central point pressure approximation	44
Figure 17.	Testing the Grauzinis method of computing directional wave spectra ..	46
Figure 18.	5 to 14 October wave and wind fields summary	50
Figure 19.	5 to 14 October horizontal velocity summary	52
Figure 20.	5 to 14 October air and sea temperatures summary	53
Figure 21.	Directional wave spectrum for 6 October 16:00 to 17:00 computed by the Grauzinis method (3D representation)	55
Figure 22.	Directional wave spectrum for 6 October 16:00 to 17:00 computed by the Grauzinis method (top view)	56
Figure 23.	Directional wave spectrum for 6 October 16:00 to 17:00 computed by the	

LCS method	57
Figure 24. Directional information for 6 October 16:00 to 17:00	58
Figure 25. Spectral functions of the sea surface elevation and horizontal velocity components for 6 October 16:00 to 17:00	59
Figure 26. Directional wave spectrum for 8 October 8:40 to 9:40 computed by the Grauzinis method (3D representation)	60
Figure 27. Directional wave spectrum for 8 October 8:40 to 9:40 computed by the Grauzinis method (top view)	61
Figure 28. Spectral functions of the sea surface elevation and horizontal velocity components for 8 October 8:40 to 9:40	62
Figure 29. Directional wave spectrum for 9 October 6:40 to 7:40 computed by the Grauzinis method (3D representation)	63
Figure 30. Directional wave spectrum for 9 October 6:40 to 7:40 computed by the Grauzinis method (top view)	64
Figure 31. Spectral functions of the sea surface elevation and horizontal velocity components for 9 October 6:40 to 7:40	65
Figure 32. Directional spectrum computed by the Grauzinis method	67

I. INTRODUCTION

A. THE PROBLEM

The need for the understanding of the kinematics of the upper ocean boundary layer has long been recognized. The motions in the upper ocean provide the means for the transfer of energy between the atmosphere and the deep ocean. The general ocean circulation has its roots in this exchange, and the understanding of the global circulation is dependent on the knowledge of the upper ocean response to the external forcing. Considerable effort has been made to characterize the fundamental mechanisms governing the kinematic behavior of the near surface ocean boundary layer. However some fundamental questions, such as the nature of the turbulence below the ocean surface, are still to be answered.

Oceanography has often followed developments by meteorologists to improve the understanding of ocean processes. However there are differences between the oceanic and the atmospheric boundary layers that do not allow parallel developments. Radiative and evaporative processes, turbulence generated by breaking surface waves, the importance of the mean flow, the dominant signal of the wave induced motions and the different scale of the phenomena all are differentiating factors.

The strong non-linear nature of the free surface boundary conditions makes the theoretical study of wave instability and the onset of breaking difficult. Breaking waves are recognized as having a primary role in the transfer of momentum, heat and gas across the air-sea interface. The large number of sources of turbulence and their overlapping characteristic frequency bands make the identification of their relative importance difficult. Moreover, the wave field has a strong signal throughout the upper ocean water column that increases the difficulty in isolating the small turbulence signal. These effects place great demands on instrumentation to measure the characteristic field variables.

B. THE OBSERVATIONAL EFFORT

The Naval Postgraduate School (NPS) participated in the SAXON experiment conducted during September and October of 1988 off the East coast of the United States. The Chesapeake Light Tower was used as a platform for investigators and instruments. The main goal of the experiment was to improve the understanding of the mechanisms responsible for SAR imaging of the ocean surface and upper ocean dy-

namics. To achieve this goal, a large set of measurements were acquired including wind stress, radar backscatter, directional wave spectra and near surface kinematics.

The instrumentation deployed by the NPS group consisted of a bistatic coherent acoustic doppler profiling velocimeter, a slope array of pressure transducers, and an electromagnetic current meter. The variables measured included two orthogonal components of the horizontal velocity field, directional wave field and the three orthogonal components of the velocity field throughout the water column. Meteorological data and wave amplitude information were measured by the Massachusetts Institute of Technology (MIT). The bistatic coherent acoustic doppler profiler velocity data are not reported, as data processing methods for this new technology are still being developed.

C. THE OBJECTIVES

The objective of this thesis is to measure and analyze the kinematics of the near surface ocean boundary layer, which is shown schematically in Figure 1. Wind and waves are the components of the forcing applied to the near surface layer. The kinematic response is represented by the velocity field, that can be thought of as being made up of two components, the mean and the fluctuating velocities. The fluctuating component of the velocity can be partitioned further into irrotational and rotational parts. The irrotational contribution is classically associated with the wave induced orbital motion, and the rotational component with the turbulence field.

In the second chapter of this thesis, linear wave theory, as representative of the irrotational component of the fluctuating velocity component is reviewed, two methods of computing directional wave spectrum are presented, and the characterization of the mean and fluctuating components of the velocity field is considered by reviewing previous theoretical and observational results. The experiment, the instrumentation deployed and their operational characteristics, and the data processing techniques are described in chapter three. Chapter four contains analysis of the results for the period 5 to 14 October with more intensive analysis for three selected one hour periods. A discussion of the results is also included in chapter four. Finally, conclusions and recommendations are presented in chapter five.

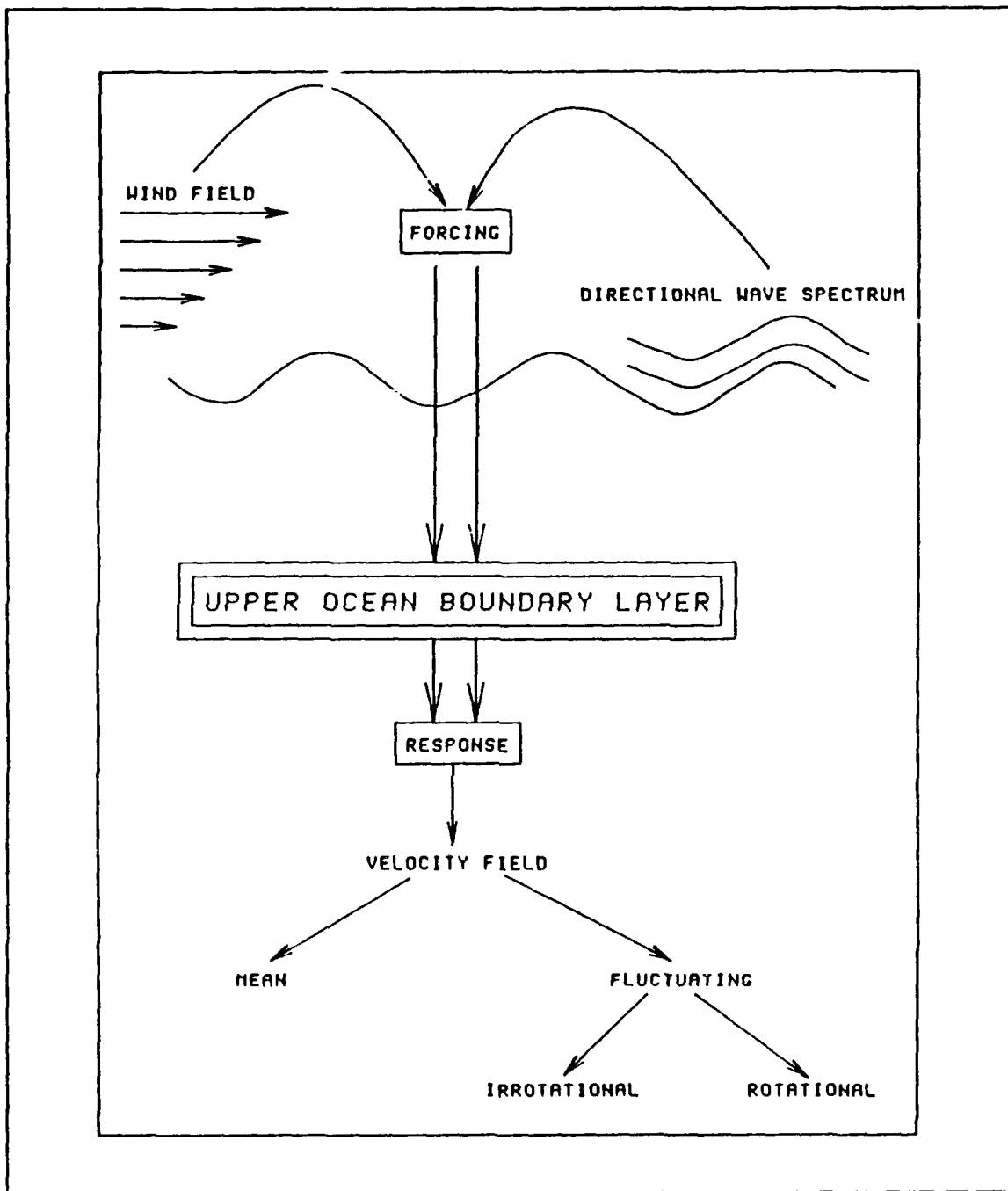


Figure 1. The Problem: The kinematic characterization of the near surface boundary layer in terms of the forcing and response components.

II. THEORETICAL AND OBSERVATIONAL BACKGROUND

A. THE LINEAR WAVE THEORY

1. Formulation

Airy or linear wave theory has been successful in describing many observed wave phenomena. In the formulation of this theory, see for instance Kinsman (1965), the basic assumptions can be summarized as

- Consideration of waves whose frequency are much greater than the earth's rotation frequency or, $\omega \gg \Omega$
- Assuming the fluid as homogeneous or, $\omega \gg N$
- Surface tension effects are negligible or, $\omega_{cp} \gg \omega$
- Considering the fluid motion as irrotational or, $\nabla \times \vec{V} = 0$, which allows the velocity potential to be defined as $\vec{V} = -\nabla\phi$
- Considering the fluid as incompressible or, $\nabla \cdot \vec{V} = 0$

where ω is the surface gravity wave frequency, Ω is the earth's frequency of rotation, N is the *Brunt - Väisälä* frequency, ω_{cp} is the frequency of the capillary waves, \vec{V} is the water particle velocity vector and ϕ is the velocity potential.

The combination of the assumptions of irrotationality and incompressibility leads to the basic equation of linear wave theory, Laplace's equation

$$\nabla^2 \phi = 0. \quad [1]$$

Analytical solutions to this equation are obtained by applying the following boundary conditions:

- Waves are periodic in space and time
- The bottom boundary is horizontal and impermeable, which is prescribed by

$$w|_{-h} = -\frac{\partial \phi}{\partial z}|_{-h} = 0 \quad [2]$$

- The linearized kinematic free surface boundary condition is expressed as

$$\frac{\partial \eta}{\partial t} - w|_{\eta} = 0 \quad [3]$$

and the linearized dynamic boundary condition as

$$g\eta - \frac{\partial \phi}{\partial t} \Big|_{\eta} = 0 \quad [4]$$

where w is the scalar vertical velocity, h is the local water depth, η is the instantaneous free surface elevation, g is the acceleration of gravity and t is time.

In the linearization process, it is assumed that the wave amplitude a is small when compared to the wavelength L and depth, or that $\frac{a}{L} \ll 1$ and $\frac{a}{h} \ll 1$. These restrictions make the linear wave theory strictly applicable to small amplitude waves of infinitesimal steepness. The resulting solution to the wave equation is a single harmonic function. Invoking the superposition principle, the instantaneous sea surface elevation can be represented as an infinite sum of sinusoids as expressed by

$$\eta(t) = \sum_{n=1}^{\infty} \eta_n = \sum_{n=1}^{\infty} a_n \cos(\vec{K}_n \cdot \vec{x} - \omega_n t + \varepsilon_n) \quad [5]$$

where \vec{K} is the horizontal vector wavenumber, $\vec{x} = (x, y)$ is the position vector, ω_n is the circular frequency and ε_n is the initial phase angle. The dispersion relationship is obtained from the solution of the wave equation in applying the surface boundary conditions

$$\omega^2 = gk \tanh(kh). \quad [6]$$

The spectral component indice n is now dropped for convenience.

The solution of the linear wave equation can be used to describe the wave induced motions. The horizontal water particle velocity component is given by

$$u(t) = \left\{ \omega \frac{\cosh k(h+z)}{\sinh kh} \right\} a \cos(\vec{K} \cdot \vec{x} - \omega t + \varepsilon) \quad [7]$$

and the vertical component given by

$$w(t) = \left\{ \omega \frac{\sinh k(h+z)}{\sinh kh} \right\} a \sin(\vec{K} \cdot \vec{x} - \omega t + \varepsilon) \quad [8]$$

where z is the depth of observation. Similarly, the pressure at a depth z can be obtained from

$$p(t) = \left\{ \rho g \frac{\cosh k(h+z)}{\cosh kh} \right\} a \cos(\vec{K} \cdot \vec{x} - \omega t + \varepsilon) \quad [9]$$

where ρ is the density. Comparing the equations [5], [7] and [9], it is readily seen that the horizontal velocity and the pressure are in phase with the instantaneous surface elevation. From equation [8] it is concluded that the vertical component of the velocity is phase advanced by 90 degrees with the sea surface elevation and the horizontal velocities when considering the vertical axis oriented positively upwards from the surface.

Two limiting regions can be considered, the deep and the shallow water wave approximations. These simplified solutions correspond to the consideration of asymptotic forms for the hyperbolic functions entering the basic solution definitions. These extreme cases are generally identified by the ratio $\frac{h}{L}$ where h is the local water depth and L is the wavelength as computed by the expressions corresponding to each one of the cases. For $\frac{h}{L} > \frac{1}{2}$ the solution is considered as belonging to the deep water limit and for $\frac{h}{L} < \frac{1}{20}$ the solution corresponds to the shallow water case. In between the full solution must be considered and the solution is known as the intermediate water wave solution.

2. Spectral and statistical relations

Open ocean data are invariably collected in the form of time series of processes that are inherently random. Spectral analysis techniques are a natural first choice to study these data. The previously presented solution to the Laplace's equation gives rise to simple spectral relationships between the sea surface elevation spectrum and velocity and pressure spectra when considering the water column as a constant parameter linear system. Under such a system, any two quantities are connected in the spectral space via a transfer function as

$$S_y(\omega) = |H(\omega)|^2 S_x(\omega) \quad [10]$$

where $S_y(\omega)$ and $S_x(\omega)$ are respectively the output and input energy-density spectra and $H(\omega)$ is the transfer function. The constant parameter linear system preserves the input frequency at the output and modifies the amplitude and phase of each component of the input independently. Similar types of relations can be deduced for the cross-spectral quantities. For the case of the open ocean wave field and considering the sea surface elevation spectra as input and the velocities or pressure as output, the applicable transfer functions are, for the horizontal velocity component

$$H_u(\omega) = \omega \frac{\cosh k(h+z)}{\sinh kh}, \quad [11]$$

for the vertical velocity component

$$H_w(\omega) = -i\omega \frac{\sinh k(h+z)}{\sinh kh} \quad [12]$$

and for the pressure

$$H_p(\omega) = \rho g \frac{\cosh k(h+z)}{\cosh kh} \quad [13]$$

Spectrally the coherence function is the measure of linear correlation between two quantities that can be thought as the input-output of a linear system. This function is obtained from the measured auto and cross-spectral density functions, and generally is considered in the form of squared coherence defined as

$$\gamma_{xy}^2(\omega) = \frac{|S_{xy}(\omega)|^2}{S_x(\omega)S_y(\omega)} \quad [14]$$

where $S_{xy}(\omega)$ is the cross spectral density function. The coherence has a value between 0 and 1, where a perfect linear relationship between input and output corresponds to the value of 1. When departures from that limiting value occur, it can be hypothesised that the process is not linear, noise is present in the measurements or there are other inputs that must be considered (Bendat and Piersol, 1986).

It was noted in the formulation of the linear wave theory that specific phase relations exist between the sea surface elevation, velocity and pressure. The relative phase between two quantities in spectral terms is defined as

$$\Phi_{xy}(\omega) = \arctan \frac{Q_{xy}(\omega)}{C_{xy}(\omega)} \quad [15]$$

where $Q_{xy}(\omega)$ is the quadrature spectrum and $C_{xy}(\omega)$ is the co-spectrum of the two quantities.

B. THE SPECIFICATION OF A WAVE FIELD

The adequate description of the wave field requires knowledge of frequency and directional wave spectra. Directional spectra are commonly measured by pitch and roll buoy and multi-element arrays, which represent spectra measured at a point. The methods for computation of the directional wave spectrum are generally classified as

- Model fitting methods - based on the parametric representation of the spectrum as the classical Longuet-Higgins et al (1963) method.
- Model independent methods (Davis and Regier, 1977), that can be divided into a priori and data adaptative methods.

A priori methods require in advance a definition of criteria to be verified without reference to the data in use. The data adaptative methods are based in a posteriori assumptions about the spectrum, which depart from characteristics of the input data. Any of these processes of estimation are conditioned by the traditional constraints inherent in time series analysis of statistical reliability and resolution.

1. Wave field description

Sea surface elevation is generally regarded as a non-deterministic random wave field. Statistical techniques must be used to define the descriptive parameters of representative data. The measurement of the fundamental properties shared by pairs of random records in the amplitude, time and frequency domains makes use of joint probability, cross-correlation and cross spectral density functions. Assuming the sea surface displacement is a stationary random function of space and time, it may be represented as, Cramer (1962),

$$\eta(\vec{x}, t) = \int_{\vec{K}} \int_{\omega} dA(\vec{K}, \omega) e^{i(\vec{K} \cdot \vec{x} - \omega t)} \quad [16]$$

where $\vec{K} = (K_x = K \cos \theta, K_y = K \sin \theta)$ represents the wavenumber vector and θ is the wave direction. From the above definition it can be shown that if $(\vec{K}, \omega) \neq (\vec{K}', \omega')$

$$\overline{dA(\vec{K}, \omega) \tilde{dA}(\vec{K}', \omega')} = 0 \quad [17]$$

and that if $(\vec{K}, \omega) = (\vec{K}', \omega')$

$$\overline{dA(\vec{K}, \omega) \tilde{dA}(\vec{K}, \omega)} = S(\vec{K}, \omega) dK d\omega \quad [18]$$

where $S(\vec{K}, \omega)$ represents the frequency wavenumber spectrum and the tilde denotes the complex conjugate. The spectral quantity [18] can be thought as the Fourier transform of the correlation function

$$S(\vec{K}, \omega) = \frac{1}{(2\pi)^3} \iint R(\vec{r}, \tau) e^{-i(\vec{K} \cdot \vec{r} - \omega \tau)} d\vec{r} d\tau \quad [19]$$

where $R(\vec{r}, \tau)$ is the correlation function defined as

$$R(\vec{r}, \tau) = E[\eta(\vec{x}, t)\eta(\vec{x} + \vec{r}, t + \tau)] \quad [20]$$

where \vec{r} is the displacement vector. From equation [19], it can be seen that under the assumption of stationarity in a homogeneous wave field the frequency wavenumber spectrum is real and positive for all \vec{K} and ω . The definition of the wave spectrum from the correlation function, equation [20], is used to relate this spectral quantity and the variance

$$\iint S(\vec{K}, \omega) d\vec{K} d\omega = \overline{\eta^2(\vec{r}, \tau)} \quad [21]$$

where the variance is proportional to the wave energy.

The frequency spectrum can be directly obtained from $S(\vec{K}, \omega)$ by integration over wavenumber

$$S(\omega) = \int S(\vec{K}, \omega) d\vec{K} = \frac{1}{(2\pi)^2} \int R(0, \tau) e^{i\omega\tau} d\tau \quad [22]$$

and the wavenumber spectrum by integration over frequency

$$S(\vec{K}) = \int S(\vec{K}, \omega) d\omega = \frac{1}{(2\pi)^2} \int R(\vec{r}, 0) e^{-i\vec{K} \cdot \vec{r}} d\vec{r}. \quad [23]$$

Using the dispersion relation as given by the linear wave theory, here considered in the deep water limit, relations can be deduced between the wavenumber, frequency and wavenumber-frequency spectra. Following Phillips (1977), it can be deduced from equation [22] that the variance is given by

$$\overline{\eta^2(\vec{r}, 0)} = \iint S(K, \theta) \frac{2\omega^3}{g^2} d\omega d\theta. \quad [24]$$

The frequency spectrum can be also obtained as the integral of the wavenumber spectrum over all directions at constant wavenumber

$$S(\omega) = \frac{2\omega^3}{g^2} \int S(K, \theta) d\theta. \quad [25]$$

This basic set of relations allows for the determination of wave field properties from the observed sea surface elevation and velocity components.

2. Directional spectrum

The summary of the wavenumber-frequency characteristics of sea waves is contained in the wave spectrum as given in equation [19]. This quantity is simply the three dimensional distribution of variance generally known as the power spectrum. The knowledge of the wave field at fixed positions (Munk et al., 1963), permits the computation of the correlation function. The definition of the power spectrum as given by equation [19] leads by inverse transforming to the correlation function, that is

$$R(\vec{r}, \tau) = \iint S(\vec{K}, \omega) e^{i(\vec{K} \cdot \vec{r} - \omega\tau)} d\vec{K} d\omega \quad [26]$$

which for the assumed stationary wave field is an even function. Consequently the power spectrum is real and symmetric about zero frequency. The correlation function can then be rewritten as a cosine transform of the power spectrum

$$R(\vec{r}, \tau) = \iint S(\vec{K}, \omega) \cos(\vec{K} \cdot \vec{r}) \cos(\omega\tau) d\vec{K} d\omega. \quad [27]$$

The correlation function can now be redefined as

$$R(\vec{r}, \tau) = \iint S(\vec{K}, \omega) (\cos(\omega\tau) \cos(\vec{K} \cdot \vec{r}) - \sin(\omega\tau) \sin(\vec{K} \cdot \vec{r})) d\vec{K} d\omega. \quad [28]$$

The power spectrum can then be calculated in terms of cosine and sine transforms of the correlation

$$S(\vec{K}, \omega) = \int [C(\vec{r}, \omega) + iQ(\vec{r}, \omega)] e^{-i\vec{K} \cdot \vec{r}} d\vec{r} \quad [29]$$

where $C(\vec{r}, \omega)$ and $Q(\vec{r}, \omega)$ are respectively the co- and quadrature spectra of the correlation. Such functions could be easily calculated if the correlation is known as a continuous function of the spatial coordinate, although real world observations lead to the

collection of data in a small number of positions. Approximate methods of computing directional spectrum from observations of the wave field at discrete positions must then be considered.

3. Classical approach

Longuet-Higgins, Cartwright and Smith (1963) (LCS) following the suggestions of Barber (1946), developed a method of computing the directional spectrum from the motions of a floating buoy. The method is based on simple relationships between the cross spectral quantities of the heave, pitch and roll of the buoy and the Fourier coefficients of the directional spectrum. The directional spectrum can be represented as a Fourier series

$$S(f) = \frac{1}{\pi} \int_0^{2\pi} e^{ni\theta} S(f, \theta) d\theta = a_n + ib_n \quad [30]$$

where θ is the wave direction and the coefficients a and b are only frequency dependent and represent the directional distribution of energy. Separating the frequency and directional contributions, as it is usually done, the directional spectrum can be rewritten as

$$S(f, \theta) = S(f)D(f, \theta) \quad [31]$$

where $D(f, \theta)$ is the spreading function. $D(f, \theta)$ corresponds to a unity area weighting function that redistributes the energy contained in the power spectrum over direction, ideally reproducing real world conditions. The three measured quantities obtained with a buoy can be directly related with the harmonic representation of the sea surface. The heave corresponds to the instantaneous sea surface elevation and the pitch and roll are associated with the spatial partial derivatives of the surface elevation. Considering a single harmonic of the sea surface representation

$$\eta(t) = a \cos(\vec{K} \cdot \vec{x} - \omega t) \quad [32]$$

the two horizontal cartesian components of the sea slope can be written as

$$\eta_x(t) = \frac{\partial \eta(t)}{\partial x} = \{-iK \cos \theta\} \eta(t) \quad [33]$$

and

$$\eta_y(t) = \frac{\partial \eta(t)}{\partial y} = \{ -iK \sin \theta \} \eta(t). \quad [34]$$

Cross spectral quantities can be computed for the instantaneous surface elevation and surface slope, and related with the Fourier coefficients of the directional spectrum. These cross spectral quantities can be represented as

$$C_{\eta\eta}(f) = S(f) \int_0^{2\pi} D(f, \theta) d\theta \quad [35]$$

$$Q_{\eta\eta_x}(f) = KS(f) \int_0^{2\pi} D(f, \theta) \cos \theta d\theta \quad [36]$$

$$Q_{\eta\eta_y}(f) = KS(f) \int_0^{2\pi} D(f, \theta) \sin \theta d\theta \quad [37]$$

$$C_{\eta_x\eta_x}(f) = K^2 S(f) \int_0^{2\pi} D(f, \theta) \cos^2 \theta d\theta \quad [38]$$

$$C_{\eta_y\eta_y}(f) = K^2 S(f) \int_0^{2\pi} D(f, \theta) \sin^2 \theta d\theta \quad [39]$$

$$C_{\eta_x\eta_y}(f) = K^2 S(f) \int_0^{2\pi} D(f, \theta) \cos \theta \sin \theta d\theta. \quad [40]$$

Considering the directional spectrum in terms of its first five Fourier coefficients, that is

$$S(f, \theta) = \frac{a_0}{2} + a_1 \cos \theta + b_1 \sin \theta + a_2 \cos 2\theta + b_2 \sin 2\theta \quad [41]$$

it can be shown that these coefficients are given in terms of the cross spectral quantities, equations [35 – 40], by

$$a_0 = \frac{1}{\pi} C_{\eta\eta} \quad [42]$$

$$a_1 = \frac{1}{\pi K} Q_{\eta\eta_x} \quad [43]$$

$$b_1 = \frac{1}{\pi K} Q_{\eta\eta}, \quad [44]$$

$$a_2 = \frac{1}{\pi K^2} (C_{\eta_x\eta_x} - C_{\eta_y\eta_y}) \quad [45]$$

$$b_2 = \frac{2}{\pi K^2} C_{\eta_x\eta_y} \quad [46]$$

and equivalently, if a normalization by auto-spectrum is done, the Fourier coefficients of the unit area spreading function are determined. This approach constitutes the classical LCS method. The approximate representation of the directional spectrum in terms of its Fourier series truncated to its first five coefficients leads to a directional distribution of energy as given by a cosine-bell function. Such a representation is of limited resolution, and typically has large negative side lobes (Figure 2).

To solve the problem of the unrealistic negative side lobes, LCS imposed a constraint of positivity on the directional spreading function which resulted in a smoothing effect. However this approach has the consequence that the resolution of a distribution narrower than $\cos^4(\frac{\theta}{2})$ is not possible. It must be noted that this artifice does not solve the real problem that is related to unresolved harmonics of the real world distribution. The under resolution is a direct consequence of the severely truncated Fourier series representation. Also, the LCS approach is not capable of representing multi-modal distributions of energy that are frequently observed in the real ocean as can be concluded from the truncated Fourier series given by [41] and shown in Figure 2.

The method just described can also be applied to measurements using slope arrays, which consist of multi-point arrangements of pressure transducers. Typically the sensors in the slope arrays are arranged in a square. The real slope is approximated by dividing the differential pressure of a pair of sensors by their separation while assuming the sea surface slope as constant between each pair of sensors. The method of computing the directional distribution of energy then proceeds as before for the case of measurements with a floating buoy. The sea surface elevation is obtained from the time series of pressure by applying the appropriate transfer function. The approximation of the surface slope introduces errors in the computation given by (Seymour and Higgins, 1977)

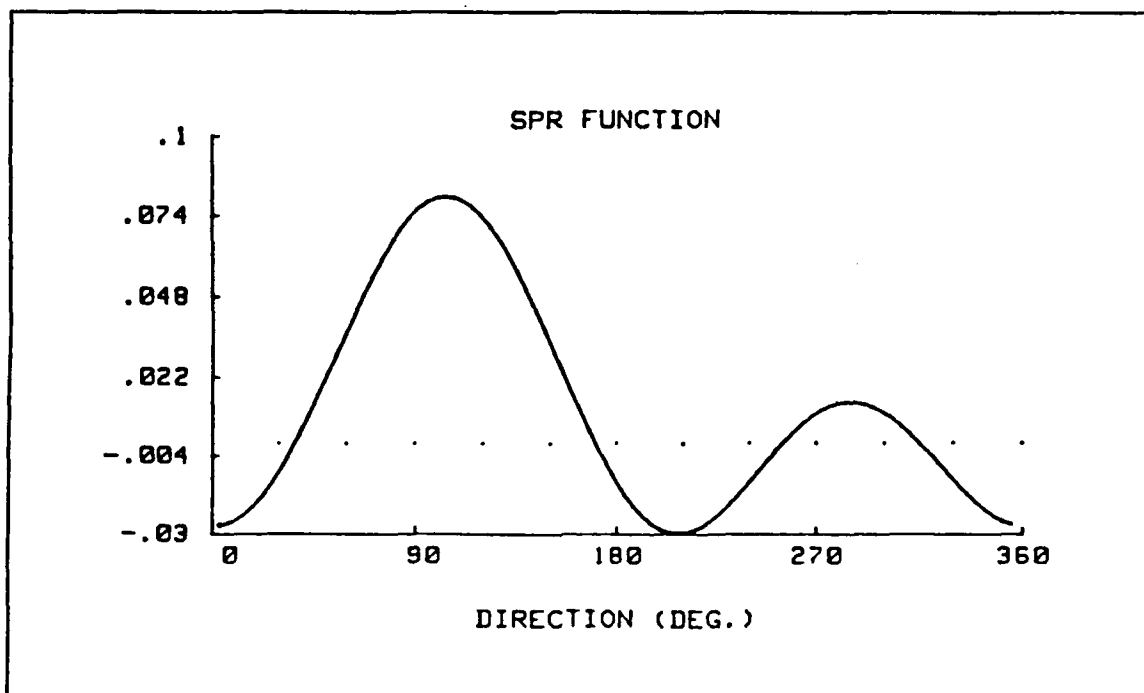


Figure 2. Typical spreading function of the LCS method: Small directional resolution and unrealistic negative side lobes.

$$\delta_i = \frac{\partial \eta}{\partial x_i} - \frac{\sin(\vec{K} A_i \alpha_i)}{\frac{\vec{K} A_i \alpha_i}{2}} \frac{\partial \eta}{\partial x_i} \quad [47]$$

where $\alpha_i = (\cos \theta, \sin \theta)$ for $i=1,2$ and A_i is the horizontal sensor separation. It can be seen that the error of such an approximation is a function of the wavenumber vector and the size of the array, decreasing in magnitude as these quantities are reduced. It is then natural to employ arrays as small as possible, limited by the resolution and accuracy of the pressure sensors.

4. Exact Fourier coefficient representation method

The LCS approach provides a way of computing the first five Fourier coefficients of the series expansion of the directional spreading function. These coefficients are obtained via cross-spectral analysis of triorthogonal components of the wave field measurements. The number of Fourier coefficients are limited because of the measurement technique normally used - floating buoy or slope array of four sensors in a square. Such a system can only give information of the wave field through second order terms.

The coefficients determined can be represented by an infinite number of different distributions whose Fourier expansion is common. Examples of distributions having the same Fourier coefficients can be seen in Figure 3. It is then natural try to choose a physically realisable distribution, which matches the coefficients determined by observation and more exactly simulates the true directional distribution.

Grauzinis (1989) exploits the matching of a set of Fourier coefficients by different distributions to develop a new method of computing directional spectra. The previously defined directional spreading function $D(\theta)$ can be represented as

$$D(\theta) = \{1 + 2 \sum_k [a_k \cos(k\theta_k) + b_k \sin(k\theta_k)]\} \frac{1}{2\pi} \quad [48]$$

where a_k and b_k are the unitary Fourier coefficients. Such coefficients enter the definition of the polar coefficients c_k and θ_k as given by

$$C_k = a_k + ib_k = c_k e^{ik\theta_k}. \quad [49]$$

Any symmetric unity area function can be determined solely by its canonical coefficients defined as

$$m_k = \int_{-\pi}^{\pi} X(\theta) \cos k\theta d\theta \quad [50]$$

where $X(\theta)$ is any arbitrary unit area function symmetric around $\theta = 0$. This representation is simply the cosine transform of an even function. It is seen that a relation can be established between the canonical coefficients and the Fourier coefficients

$$a_k + ib_k = c_k e^{ik\theta_k} = m_k e^{ik\beta_k} \quad [51]$$

where the polar form is now used for the Fourier coefficients of the spreading function. Using linear superposition, any unit area function can be reproduced by a weighted sum of symmetric unit area density functions oriented at different directions as given by

$$c_k e^{ik\theta_k} = \sum_j w_j m_k(j) e^{ik\beta_j} \quad [52]$$

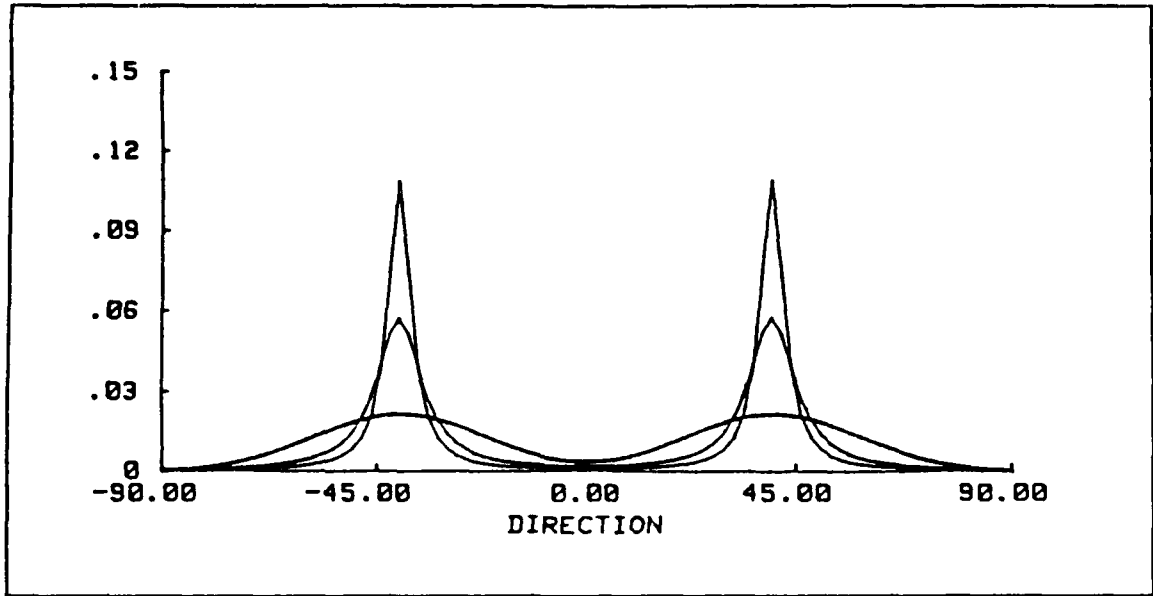


Figure 3. Distributions of energy: The three distributions have a common Fourier expansion.

where w_j is the weighting factor and β_j is the orientation of each of the components considered in the series. Equation [52] constitutes the generating equation for the polar coefficients where on the right hand side w_j , $m_i(j)$ and β_j are unknowns. The left hand side of [52] is determined from the cross spectral quantities of the wave field typically known through second order. A system of equations can be established as

$$m_1[w_1 e^{i\beta_1} + w_2 e^{i\beta_2}] = c_1 e^{i\theta_1} \quad [53]$$

$$m_2[w_1 e^{i2\beta_1} + w_2 e^{i2\beta_2}] = c_2 e^{i2\theta_1} \quad [54]$$

which can be seen to be underdetermined. It must be noted that in the system [53 – 54] it is assumed that the canonical coefficients are common to both of the distributions of energy considered. This was the approach followed by Grauzinis (1989) to obtain analytic solutions for the system of generating equations. By the fortunate condition of orthogonality of the exponentials of different order and the side condition that the sum of the weights must be equal to unity, analytic solutions are formed. The analytic solutions constitute an implicit underdetermined system of four equations. The unknowns of this system are the two canonical coefficients, the orientation of the two unit area density functions and one of the weighting functions. To solve this system,

further constraints are needed. Assuming a functional relationship between the canonical coefficients m_1 and m_2 particular solutions are obtained. The original relationship adopted was a power law between the two canonical coefficients

$$m_2 = m_1^r \quad [55]$$

that for different values of r originated different distributions of energy as analytic solutions. Such distributions are of decreasing sharpness as the magnitude of the exponent increases. For the values of the exponent 2, 3 and 4, the resulting distributions in its unimodal form are represented in Figure 4, for two different values of the canonical coefficient. The introduction of two distributions of different orientations and weights allows this method to represent bimodal distributions of energy. Also the variable sharpness of the model distributions considered will permit the matching of observed distributions of considerable more peakedness than the classical LCS method. For a canonical coefficient of .9 the half-power width of the distribution D4 is 12 degrees, that is about one-third of the typical resolution of the cosine-bell distribution.

Knowledge of Fourier coefficients of order higher than the second introduces considerable advantage to this method. Some of the constraints can be dropped, such as the functional relationship of the canonical coefficients. Moreover, the matching of coefficients of higher order increases the resolution of the method.

The exact matching of the Fourier coefficients through second order of any spreading function can be obtained by the method just described. The problem of what criteria to use for the selection of the distribution that best matches the real data must also be considered. It should be emphasized that there exist an infinity of distributions that can be considered to match the same set of Fourier coefficients. The problem of selecting the best fitting distribution partly amounts to the matching of the ocean peakedness. Cartwright (1963) considered this problem when computing directional wave spectra by the LCS method. He concluded that information could be obtained from the ratio of the magnitude of the coefficients C_k , [49]. The magnitude of such coefficient is given by

$$C_k = \sqrt{a_k^2 + b_k^2} \quad [56]$$

Recalling the functional relationship of the canonical coefficients introduced to allow for the solution of the generating system, [55] it is concluded that in the Grauzinis method

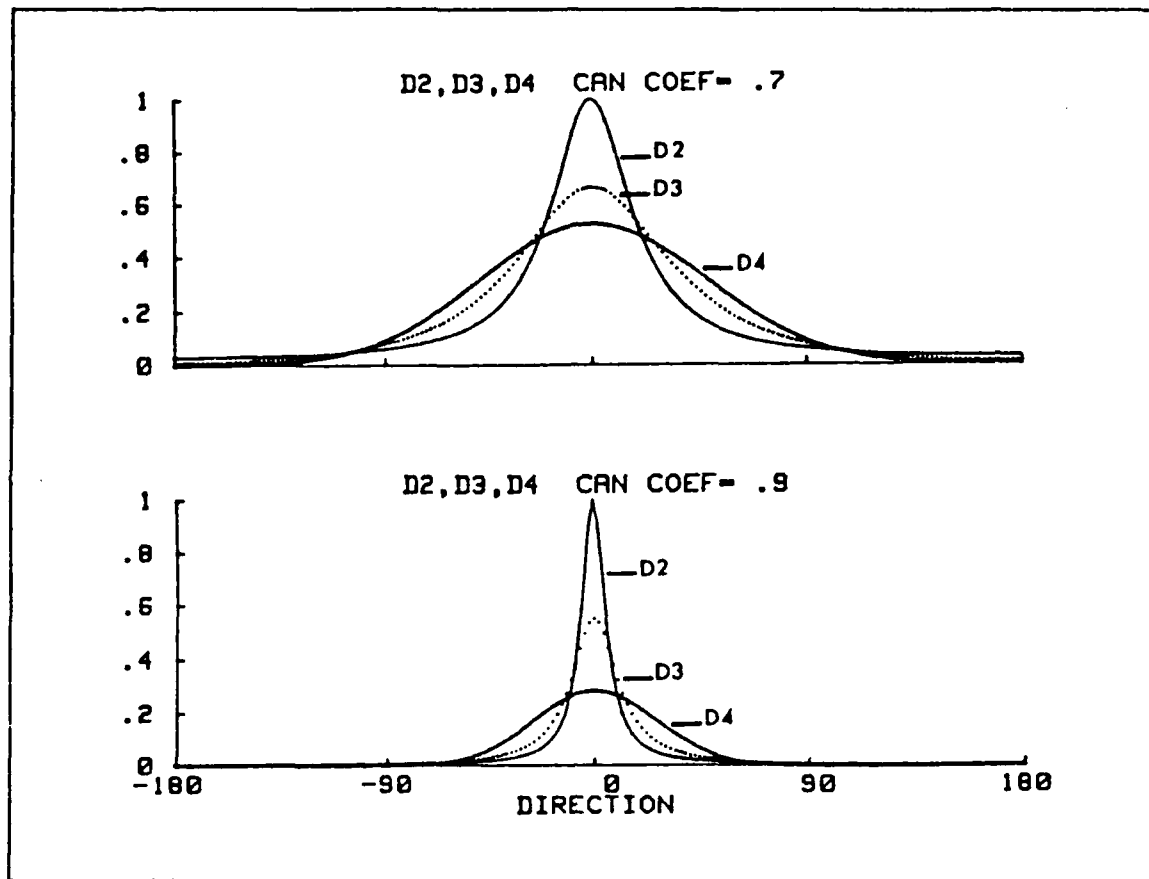


Figure 4. Three model distributions: Uni-modal representation of three different model distributions for two values of the canonical coefficient. D2 , D3 and D4 correspond respectively to the exponent 2, 3 and 4 for the functional relationship of the canonical coefficients [55] . The sharpness of the distribution increases with the magnitude of exponent. For a value of the canonical coefficient equal to .9 the half power width of D4 is 12 degrees.

it is more natural to consider the ratio of the natural logarithms of the C_i coefficients, that is

$$LogRatio = \frac{\ln(C_2)}{\ln(C_1)} \quad [57]$$

which represents the greatest power-law of the canonical coefficients that can match the input Fourier coefficients. Cartwright (1963) verified that the ratios obtained from the observed data were consistently greater than the values corresponding to the cosine-bell function of the LCS method. It was hypothesized that such difference could be due to the multimodality of the wind-wave spectrum. Recalling that the ratio of the coefficients C_k as an indicator was deduced from uni-modal considerations, it does not seem correct to make use of it to infer of the adequacy of multi-modal distributions. Grauzinis (1989) points out that the natural logarithmic ratio will exceed the power law of the canonical coefficients increasingly as the beam separation gets larger¹. Moreover, the noise affects the coefficients C_2 and C_1 differently. Equations [42 – 46] show that the effects of noise are cancelled for the coefficient a_2 , and consequently the LogRatio will be decreased.

Grauzinis (1989) proposes the Beam Separation Index (BSI) as an indicator of the best fitting distribution. This measure is deduced from the analytic solutions of the generating system by considering the canonical coefficients that would make the beam separation zero for a given set of coefficients. The BSI has a zero value in the unseparated canonically matched situation, and provides a relative measure of canonical fitting with least beam separation. From the definition of the BSI, it is concluded that the matching of broad distributions of energy will result in bigger values of the index, corresponding to sharper model distributions. The BSI is a better indicator of the best fitting distribution than the LogRatio. BSI by definition contrasts parameters of the real data with model parameters, rather than exclusively data parameters, as is the case for the LogRatio. However, it must be emphasized that the canonical coefficients used for the comparison correspond to constrained analytic solutions, so that only a relative measure is obtained.

C. THE VELOCITY FIELD

1. Means and fluctuations

The ocean is constantly being fed momentum by the wind. Although several theories exist that try to explain the transfer mechanism, the exact coupling is not known. To understand the way momentum is injected into the ocean through the air-sea interface and to look for its depth penetration in the water column, it is necessary to examine and characterize the upper ocean velocity field. To gain insight, the velocity field is often partitioned into mean and fluctuating parts and expressed as

¹ The beam separation is defined as the angle between the orientations of the two unit area model density functions.

$$v = \bar{v} + v' \quad [58]$$

where v is the total observed field, \bar{v} is the mean component and v' is the fluctuating part. The fluctuating part can be further partitioned into the wave and turbulent contributions

$$v' = v_w + v_t \quad [59]$$

where subscripts w and t refer to the wave and the turbulent components. The fluctuating part is random in nature and only treatable statistically. An objective is to separate the two parts of the total field spectrum in order to define the scales, and isolate the spectrum of interest. Such separation is usually done by an averaging process that must be capable of maintaining the coherence between the separated parts and the corresponding equations of motion. In fact, an incoherent averaging process can result in the loss of understanding of the phenomena. To avoid such an undesirable situation the method must verify a basic set of requirements that can be summarized (Panofsky and Dutton, 1984) as follows

- The averages obtained must be differentiable to any order as required by the equations of motion
- The Reynolds' postulates must be verified.

The Reynolds' postulates are generally presented as

- The fluctuations must have a zero average, or $\bar{v}' = 0$
- The correlation between the mean and the fluctuating parts must vanish, or $\overline{v'v} = 0$
- A mean quantity must be unchanged by an averaging process or, $\bar{\bar{v}} = \bar{v}$.

Meeting all the requirements makes the averaging process non-trivial, and it can be shown that the only way to completely satisfy all the requirements is to ensemble average. Ensemble averaging is not applicable to the length restricted series that constitute the generally available data sets. Other processes are then required. Alternatives to the ensemble average include time averages over discrete periods, fitting linear regression equations to nonoverlapping samples of the time series, moving averages and harmonic analysis techniques. All these processes violate to some extent the requirements mentioned above, but as Lumley and Panofsky (1964) have shown, the situation is improved if a gap is present in the spectra of the phenomena.

2. The mean velocity field

The mean component of the total velocity field is at least in principle the easiest to characterize, since deterministic relations are expected to completely describe it. Ekman (1905) pioneered this study. Following the suggestions of Nansen, a constant viscosity model of the turbulent friction was used. The solution obtained is a steady spiral turn of the currents to the right of the wind (Northern Hemisphere) with increasing depth. The key result of the Ekman layer theory can be presented as

$$\vec{M}_E = \frac{\vec{\tau}_0 \times \vec{e}_3}{\rho f} \quad [60]$$

in which the net-transport, \vec{M}_E , in a steady, linear Ekman boundary layer flows 90 degrees to the right of the applied wind stress, $\vec{\tau}_0$, and has a magnitude of $|\tau_0(\rho f)^{-1}|$ regardless of the vertical distribution of stress as long as it vanishes at some depth. In the above definition, f is the Coriolis parameter and \vec{e}_3 the vertical unit vector. The parametrization of the near-surface stress in terms of an assumed constant eddy viscosity constitutes the weak point of this theory, since turbulence in nature varies considerably in space and time.

Prandtl (1925) introduced the mixing-length theory to describe turbulent effects in the mean flow (see for instance Holton, 1979). The basic idea is the parametrization of the small-scale eddy motions in terms of the large scale mean flow. The primary hypothesis is that in a boundary layer a parcel of fluid which is displaced away from the solid boundary will carry the mean horizontal momentum of the original level, and that after moving a characteristic distance, analagous to the mean free path in molecular viscosity, the parcel of fluid will transfer the excess of momentum at the new level, creating a turbulent velocity fluctuation. The velocity fluctuation is proportional to the free path and to the shear of the mean velocity. In the boundary layer, the velocity scale is given by the friction velocity defined by $u_* = \sqrt{(\frac{\tau}{\rho})}$. The relevant length scale is the distance of the particle from the solid boundary. The mean velocity gradient is expressed as

$$\frac{\partial \bar{u}}{\partial z} = \frac{u_*}{\kappa z} \quad [61]$$

and when vertically integrated leads to the well known logarithmic velocity profile

$$\bar{u} = \frac{u_*}{\kappa} \ln\left(\frac{z}{z_0}\right) \quad [62]$$

where κ is the von Karman's constant and z_0 is called the roughness parameter. This law holds quite accurately in constant stress layers.

Bye (1965) made observations of the wind driven circulation in the vertical plane of an unstratified lake of constant depth using wooden floats of variable lengths. Considering the translational velocity of the floats as representative of the vertically averaged current in which they drift, measurements were made in the first meter of the water column. The observations showed that the near surface currents were logarithmically distributed in good agreement with the conclusions of the mixing length theory.

Wu (1975) performed measurements of the wind induced currents in a wind-wave tank, and several wind conditions were simulated. The data were collected by tracking submerged wooden floats and also by using a Pitot-static tube that was placed at selected depths. The total drift current was considered as representing the wind induced current, since Wu concluded that the Stokes' drift was negligible. The results obtained showed a logarithmic Prandtl type distribution for the current near the surface while, for the region immediately below the surface, the current varied linearly with the depth, consistent with the existence of a viscous sub-layer. The results obtained by Wu are presented in Figure 5.

Churchill and Csanady (1983) measured near surface water currents in the coastal zone of Lake Huron and Cape Cod Bay by tracking drifters and drogues both visually and acoustically. The observed near surface currents showed a nearly logarithmic variation with depth to about 1 meter below the surface. The direction of the currents was almost parallel to the wind and predominant wave direction. Figure 6, shows a typical profile obtained from the measurements. For this experiment, the roughness parameter was calculated by relating the velocity profile projected to the surface velocity. The estimated values of the roughness parameter were considerably larger than typical values on the air side for similar wind conditions. The conclusions obtained by Churchill and Csanady about the roughness parameter are quite different than those of Wu, who concluded that the roughness length was smaller in the water than in the air in low wind velocities and much smaller under high wind velocities. For a similar wind condition, Wu shows values of the roughness parameter of the order of a few millimeters, while Churchill and Csanady computed a roughness length of the order of ten's of centimeters.

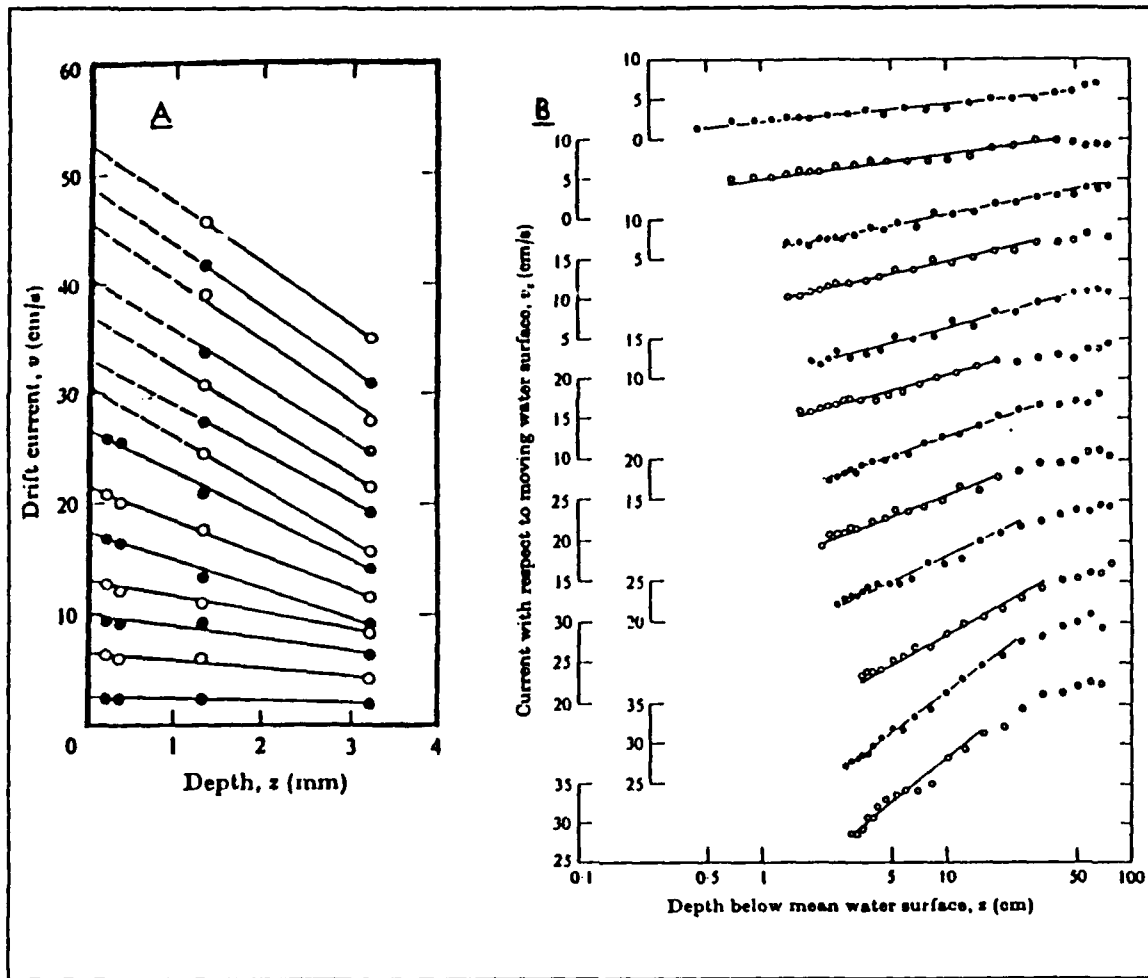


Figure 5. Mean drift current profiles after Wu: (a) From bottom to top the currents were obtained in order of increasing wind velocity. The constant shear is consistent with the existence of a viscous sub-layer. (b) Near surface drift current relative to the moving water surface. Depth scale is logarithmic. The suggested profile agrees with a Prandtl-Karman type profile. Adapted from Wu (1975).

Richman, De Szoeke and Davis (1987) used a string of vector-measuring current meters suspended beneath a surface float to assess the near surface shear. Their results show that the observed shear is consistent with the results of the mixing-length theory, given by $u_* (\kappa z)^{-1}$ for a layer of about 5 meters. The velocities differences between 2.5 and 5.5 meters depth as observed and the values estimated by the logarithmic profile law are

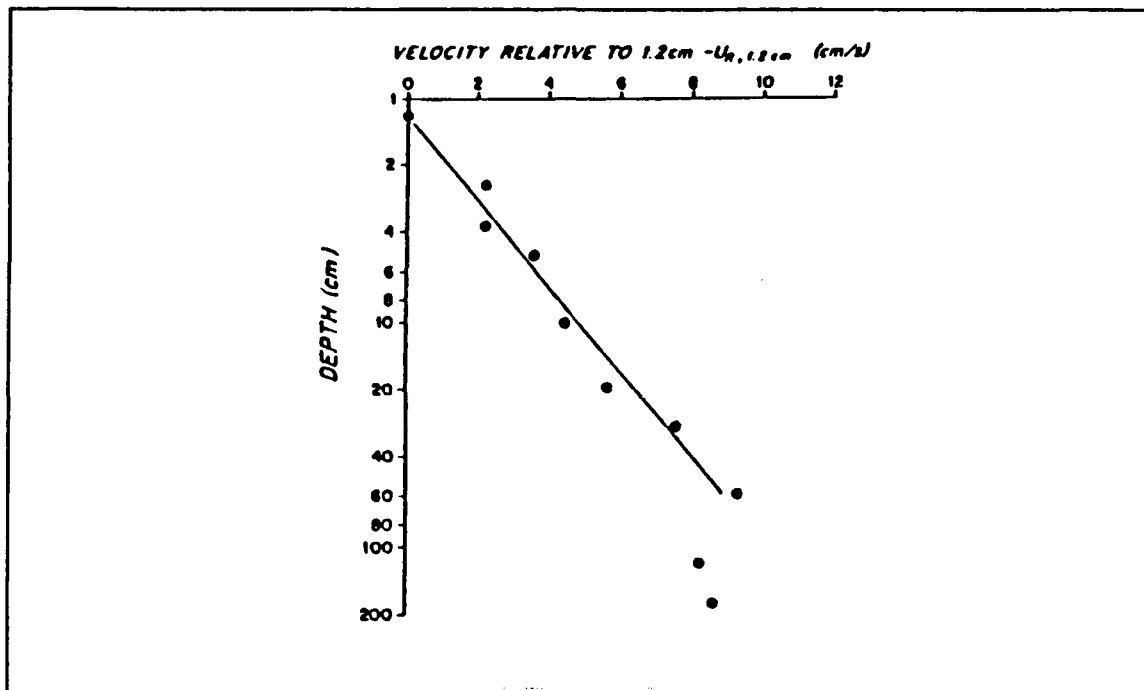


Figure 6. Mean velocity profile after Churchill and Csanady: Typical profile from drifter and drogue data of velocity relative to 1.2 cm is plotted against depth (logarithmic scale). The line corresponds to a least squares linear regression. Adapted from Churchill and Csanady (1983).

shown in Figure 7. A clear change of the current direction with depth was also observed. From a downwind logarithmic profile, the mean flow evolved to a rightward turning profile consistent with Ekman theory (Figure 7). The transition for the two regimes occurs, for these observations, at depths that scale with $\frac{u_*}{f}$.

From the diverse set of studies presented, the mean velocity field in the upper ocean mixed layer appears to be characterized by

- A region close to the surface where the velocity variation with depth is linear, and thus consistent with the existence of a viscous sublayer. In such region the constant velocity gradient can be related to the stress by

$$\frac{\partial \bar{u}}{\partial z} = \frac{u_*^2}{\nu_e} \quad [63]$$

where ν_e is the effective viscosity.

- A lower region where the velocity varies logarithmically with depth consistent with the Prandtl-Karman profile.

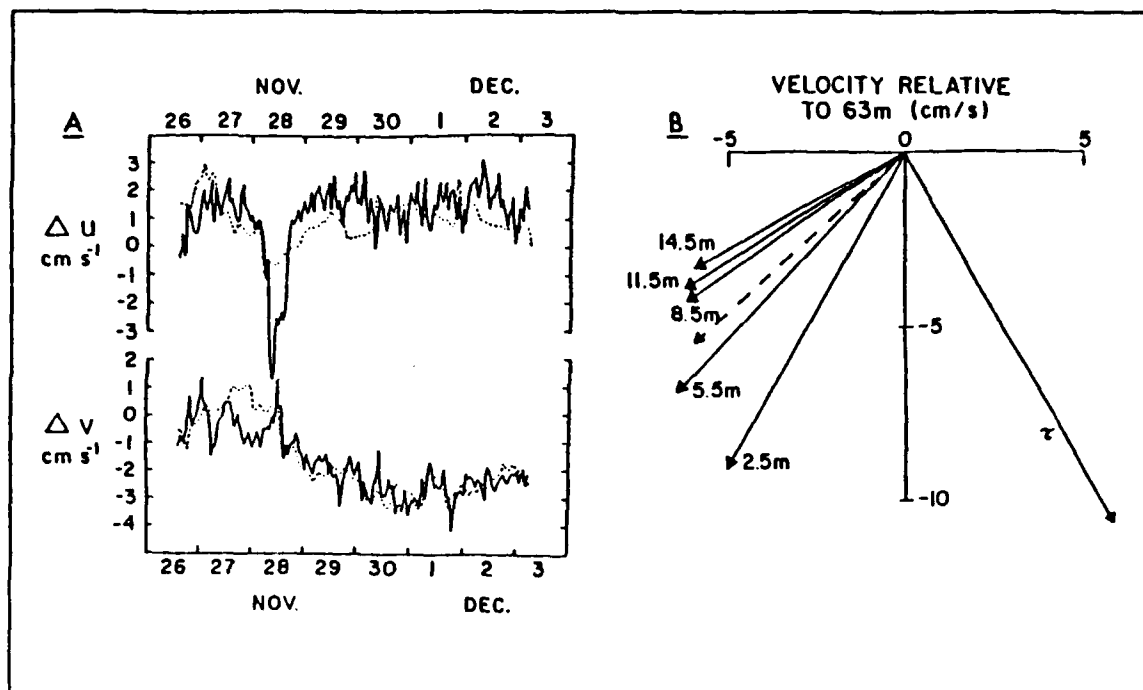


Figure 7. Mean velocities in the upper ocean boundary layer after Richman et al.: (a) Velocity differences between 2.5 and 5.5 meters depth (solid line) compared to the logarithmic profile law (dashed line). (b) Mean flow relative to 63 meters depth. τ is the mean wind stress vector. The mean flow turns to the right of the wind stress with depth increase. Adapted from Richman et al (1987).

- Below these upper regions a layer where the rightward turning profile occurs as predicted by the Ekman theory.

The scales of each of the layers are strongly dependent on the wind forcing. The different conditions of the experiments do not allow for a clear comparison of the results.

3. The fluctuating field

The fluctuating component of the total velocity field is more complex than the mean component. Two primary reasons lead to its complexity and lack of understanding:

- the great number of sources of variability and the inherent non-linearity of the coupling processes, and
- the difficulty in separating small turbulent signals in the presence of a strong wave signal

The real world fluctuations in the near surface can be associated with the ocean surface waves in the form of orbital velocities observed in a frequency band above approximately 10^{-1} Hz. Breaking events and other non-linear wave interactions will lead to a transfer of energy away from the principal frequencies. Such a transfer can be directed both toward high and low frequencies. Wave interactions result in associated energy transfer processes that covers a wide band of wavenumbers. The Coriolis force can cause inertial fluctuations of the currents in the mixed layer. Internal waves constitute another source of variability, and the frequencies associated are typically near 10^{-2} Hz, that is, below the *Brunt – Väisälä* frequency. Tidal motions must also be considered with the highest frequency of about 12 hours resulting in a frequency band overlapping with the band of inertial oscillations. Besides all these, one must account for the shear stress carrying eddies. The overlapping of the frequency bands is in fact the big problem for the individual characterization of the contributions.

Particular attention has been given to the kinematics of the water particles under wind waves. Considering wind waves as the primary source of fluctuations reduces the range of frequencies to analyze. The range of frequencies will be restricted to the region where the sea and swell make their appearance, that is frequencies of the order of about 10^{-1} Hz and above. Classically, a distinction has been made between the fluctuations associated with the orbital motions of the waves and the "other" contributors, these being generally referred to as turbulent sources.

4. Velocity field and surface elevation

As previously noted, linear wave theory allows the description of the wave induced motion at any depth. For such estimation, the knowledge of the basic wave field characteristics of wave height H , wave period T and the local water depth h are required. Under the assumptions of stationarity and uniformity, it is possible to compute the auto and cross spectra of the surface elevation and the velocity components. From the spectral relationships, important conclusions can be drawn.

The fluctuating field can be considered as the superposition of the wave and turbulent components. The wave component is generally considered as the irrotational part of the fluid motion, described by the linear wave theory. The turbulent component is essentially rotational in character. Seitz (1971) concluded that the total water particle motion at depth could be considered as the sum of the wave induced motion and turbulent motion, with the turbulent motion being all that was not wave related. This model was obtained by comparing a measured velocity spectrum with the one obtained by directly measuring the surface wave field.

The spectrum of the vertical component of the velocity can be expressed in terms of the wave and turbulent components as

$$S_w(\omega) = S_{w_w}(\omega) + S_{w_t}(\omega) + S_{w_w w_t}(\omega) + S_{w_t w_w}(\omega). \quad [64]$$

Under the assumption of statistical independence between the wave induced and turbulent velocity components, their cross spectral quantities are identically zero and the spectrum of the vertical velocity can be simplified to

$$S_w(\omega) = S_{w_w}(\omega) + S_{w_t}(\omega) \quad [65]$$

which allows the separation of the turbulent component to be considered as given by

$$S_{w_t}(\omega) = S_w(\omega) - S_{w_w}(\omega) \quad [66]$$

that is, defined in terms of measurable quantities. The wave induced velocity can be obtained from the measured sea surface elevation via the transfer function. Moreover, the assumption of statistical independence between the wave induced velocity and the turbulent component allows for the representation of the cross spectrum between surface elevation and the vertical component of velocity as

$$S_{w\eta}(\omega) = S_{w_w\eta}(\omega) \quad [67]$$

where the contribution by the turbulent component is now zero. The coherence function between the surface elevation and the vertical component of the wave induced velocity is unity under the assumption of a constant parameter linear system, or

$$\gamma_{w_w\eta}^2(\omega) = \frac{|S_{w_w\eta}(\omega)|^2}{S_{w_w}(\omega)S_{\eta}(\omega)} = 1. \quad [68]$$

By definition of the coherence function for the total vertical velocity and sea surface elevation and using [65], [67] and [68]

$$\gamma_{w\eta}^2(\omega) = \frac{S_{w_w}(\omega)S_{\eta}(\omega)}{(S_{w_w}(\omega) + S_{w_t}(\omega))S_{\eta}(\omega)} \quad [69]$$

which can be simplified to

$$\gamma_{w\eta}^2(\omega) = \frac{S_{w_w}(\omega)}{S_{w_w}(\omega) + S_{w_t}(\omega)} = \frac{S_{w_w}(\omega)}{S_w(\omega)}. \quad [70]$$

From [70] it is noted that the coherence function between the vertical component of the velocity and the sea surface elevation is independent of the directional distribution of wave energy.

Considering the wave induced and the turbulent components of the velocity as correlated adds complexity to the problem. From the definition of the spectrum of the total velocity field [68], the turbulent component is given by

$$S_{w_t}(\omega) = S_w(\omega) - S_{w_w}(\omega) - S_{w_w w_t}(\omega) - S_{w_t w_w}(\omega) \quad [71]$$

where the cross spectral quantities cannot be directly obtained from field measurements. Separating the turbulent and wave induced parts in the definition of the total velocity field [75], the spectral turbulent density function is given by

$$S_{w_t}(\omega) = S_w(\omega) - S_{w_w}(\omega) - S_{w_w w_t}(\omega) - S_{w_t w_w}(\omega) \quad [72]$$

where all the quantities are now related to the total and the wave induced velocity field. The spectral density of the wave induced velocity can be written as

$$S_{w_w}(\omega) = |H_w(\omega)|^2 S_\eta(\omega) \quad [73]$$

and the cross spectral density function of the wave induced and the total velocity field as

$$S_{w_w w_t}(\omega) = \tilde{S}_{w_w w_t}(\omega) = \tilde{H}_w(\omega) S_{\eta w_t}(\omega) = \tilde{H}_w(\omega) \tilde{S}_{w_t \eta}(\omega). \quad [74]$$

The spectrum of the turbulent velocity component [76] can now be rewritten as

$$S_{w_t}(\omega) = S_w(\omega) - |H_w(\omega)|^2 S_\eta(\omega) - \tilde{H}_w(\omega) S_{\eta w_t}(\omega) - \tilde{H}_w(\omega) \tilde{S}_{w_t \eta}(\omega) \quad [75]$$

or equivalently

$$S_{w_t}(\omega) = S_w(\omega) - |H_w(\omega)|^2 S_\eta(\omega) - 2\text{Re}\{H_w(\omega) S_{w_t \eta}(\omega)\} \quad [76]$$

and the last term takes the form

$$\text{Re}\{H_w(\omega)S_{w\eta}(\omega)\} = |H_w(\omega)|Q_{w\eta}(\omega). \quad [77]$$

Using the relations now derived, the coherence function between the total velocity field and the sea surface elevation is given by

$$\gamma_{w\eta}^2(\omega) = \frac{|S_{w\eta}(\omega) + S_{w,\eta}(\omega)|^2}{\{S_{w,\eta}(\omega) + |H_w|^2 S_{\eta}(\omega) + 2|H_w(\omega)|Q_{w\eta}(\omega)\}S_{\eta}(\omega)} \quad [78]$$

and it is immediately concluded that the coherence value is greater than for uncorrelated wave induced and turbulent components of the total velocity field. For statistical independence between those two components, the cross spectral quantity of the turbulent velocity field and surface elevation will be identically zero with all the other quantities entering the definition of the coherence for the correlated case remaining unchanged.

The coherence function between the horizontal velocity component and the sea surface elevation can be formed as

$$\gamma_{v\eta}^2(\omega) = \frac{S_{v_w}(\omega)}{S_{v_w}(\omega) + S_{v_t}(\omega)} = \frac{S_{v_w}(\omega)}{S_v(\omega)} \quad [79]$$

for statistical independence between the wave induced and turbulent components. The horizontal velocity is defined in terms of its cartesian coordinates as

$$\vec{u} = \vec{u}_{w_x} + \vec{u}_{w_y} + \vec{u}_t \quad [80]$$

where isotropy is assumed for the turbulent velocity component. In [80], w represents the wave component. The directivity of the waves must be accounted for when considering the horizontal velocities. Recalling the definition of the frequency wave spectrum

$$S_{\eta}(\omega) = \int_{\theta} S_{\eta}(\omega, \theta) d\theta \quad [81]$$

and the transfer function as given by the linear wave theory, the coherence function for the horizontal velocity components and sea surface elevation can be written as

$$\gamma_{u,\eta}^2(\omega) = \frac{|H_u(\omega)|^2 \int_{\theta} \cos^2 \theta S_{\eta}(\omega, \theta) d\theta}{|H_u(\omega)|^2 \int_{\theta} \cos^2 \theta S_{\eta}(\omega, \theta) d\theta + S_{u_t}} \quad [82]$$

and

$$\gamma_{u,\eta}^2(\omega) = \frac{|H_u(\omega)|^2 \int_{\theta} \sin^2 \theta S_{\eta}(\omega, \theta) d\theta}{|H_u(\omega)|^2 \int_{\theta} \sin^2 \theta S_{\eta}(\omega, \theta) d\theta + S_{u_t}} \quad [83]$$

with $H_u(\omega)$ given by [11]. It is evident from the definitions of $\gamma_{u,\eta}^2(\omega)$ and $\gamma_{u,\eta}^2(\omega)$ that they are dependent on the bivariate wave spectrum, which differs from the coherence function between the vertical component of the velocity and the sea surface elevation.

Definitions [70], [82] and [83] show that a decrease in coherence will result as a consequence of an increased ratio of the turbulent to the wave component. Such situations will be particularly true for deeper positions in the water column, since the wave induced component is proportionally reduced. This process of filtration by depth is frequency selective with the coherence function reducing faster in the high frequency region of the spectrum. It can be hypothesized that the energy content of an observed spectrum for which the coherence function between surface elevation and velocity shows small values, is primarily turbulent when assuming statistical independence between the wave induced and turbulent components of the total velocity field, negligible measurement noise, and a completely linear wave field.

Yefimov and Khristoforov (1971) have investigated the behavior of the coherence function of the velocity field and surface elevation assuming statistical independence between the wave induced and turbulent part of the total velocity field. They considered a minimum level of coherence, and define that above the frequency where such value is observed, the vertical velocity fluctuations become decoupled from the surface elevation. The velocity is then assumed to be not primarily wave related, but turbulent in nature. Observations have shown that the transition frequency, defined ac-

According to the above criteria, shifts to the lower frequency as depth of measurement below the surface increases, as would be expected. Such shifting can be observed in Figure 8, and shows the relative increase of the turbulent content towards the shorter scales. This situation, apart from the depth filtration of the wave induced components, can be related to turbulence convected by the mean flow, and as such is independent of locally generated turbulence. When analysing the horizontal component of the velocity, it was observed that the coherence values were consistently smaller than the values obtained when considering the vertical component. Also, the transition frequency was lower than in the previous case. Such smaller values can be associated with an increase of the turbulent component relative to the wave energy, that has in this case a preferential orientation. It can be hypothesized that there is a considerable transport of horizontal momentum by the vertical component of the fluctuating field, which will lead to an increase of the critical ratio of turbulent wave energy. The directional spreading of the real wave field must also be considered ([82] and [83]). Yefimov and Khristoforov concluded that the spectrum of the vertical velocity could be considered as the sum of a wave and a turbulent spectrum, since the wave induced component was verified to be well reproduced by estimation according to linear wave theory.

Thornton and Kraphol (1974) measured the waves using a wave staff and the two orthogonal particle velocities, vertical and horizontal, using an electromagnetic current meter. It was concluded from the observations that there was a high correlation between the surface elevation and the vertical component of the velocity in the energetic wave band. The limit of high wave energy fluctuations was established in the study by Thornton and Kraphol as the frequency where the velocities observed and theoretically deduced by linear theory become significantly different. As observed by Yefimov and Khristoforov the upper limit of high coherence decreased with increasing depth (Figure 9). The horizontal velocity and the sea surface elevation showed a smaller value for the coherence, which also agrees with the results of Yefimov and Khristoforov.

The phase relations predicted by linear theory between the vertical and horizontal velocity components have been considered by Shonting (1970). Time series of horizontal and vertical velocity components of motion beneath the ocean free surface were measured using orthogonally mounted ducted meters. The cross spectrum of the horizontal and vertical components show (Figure 10) disagreement with the expected values of linear wave theory. A phase difference of 90 degrees would be expected from theory, and consequently their co-spectrum should be ideally zero over the energetic

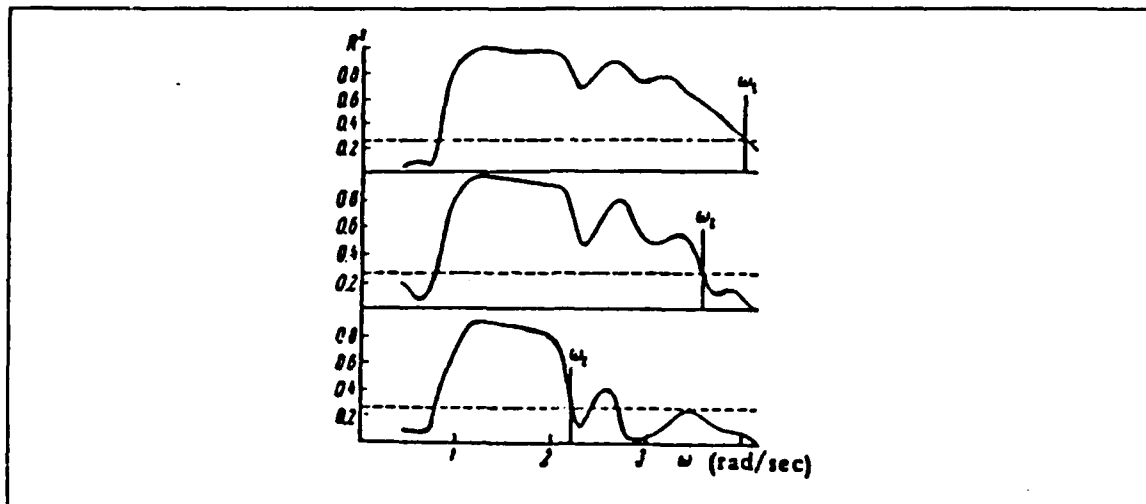


Figure 8. Coherence function between the sea surface elevation and the vertical component of the fluctuating velocity field after Yefimov and Khristoforov: The coherence decreases in the high frequency range and the transition frequency ω , shifts towards the low frequency with depth increase. Plots refer to increasing depth from top to bottom. Adapted from Yefimov and Khristoforov (1971).

band of frequencies. The values of the co-spectrum are 20 percent of the magnitude of the quadrature spectrum indicating a significant departure from predictions.

Thornton and Kraphol (1974) found measured phase differences between waves and velocity components (Figure 11) of around 90 degrees in the band of significant wave energy, which is consistent with the linear wave theory. The phase relations of the horizontal velocity and surface elevation spectra given by linear wave theory were similarly confirmed (Figure 11).

Cavaleri and Zechetto (1987) also focused their attention on the phase relationship between surface elevation and the velocity components. In an experiment conducted in the Adriatic Sea, the velocity field data were measured using electromagnetic current meters placed at right angles and the sea surface elevation was measured using pressure transducers and resistance wave gauges. Their results (Figure 12) are very close to those obtained by Shonting (1970). While the vertical velocity component closely followed a quadrature relation with the surface elevation, the horizontal component is significantly different from the predicted in phase condition with

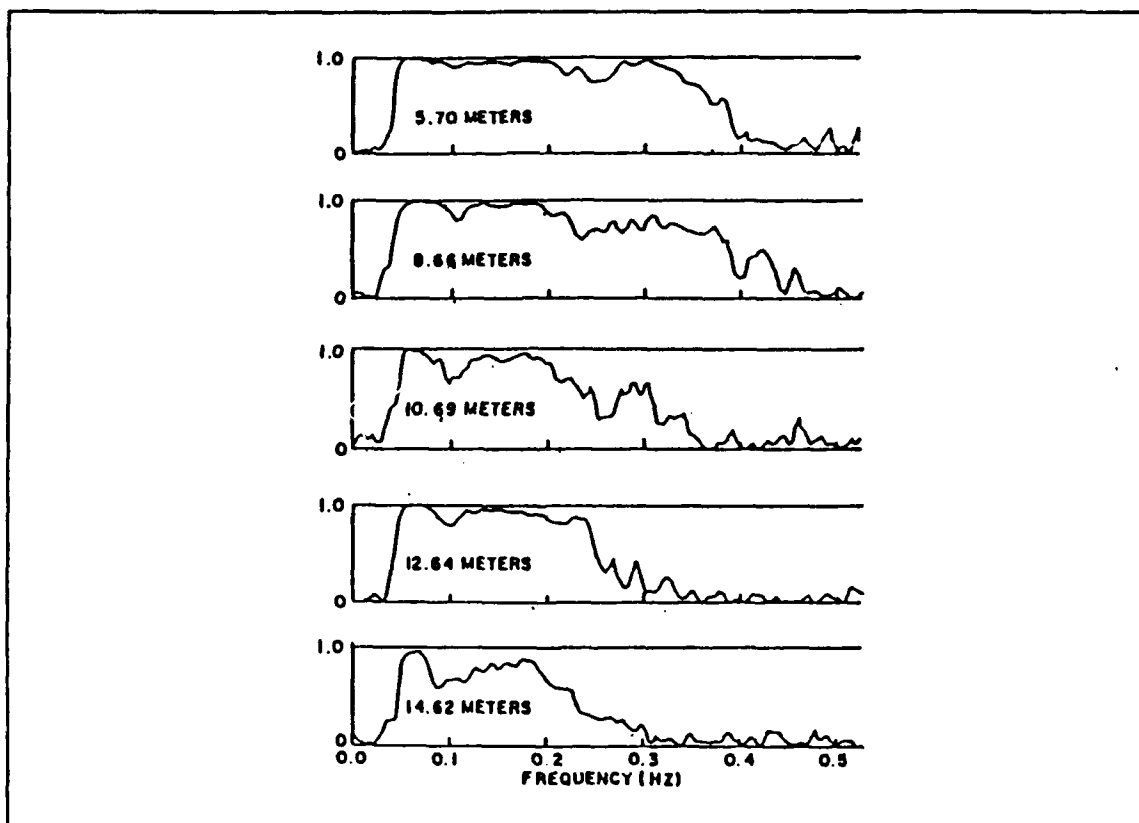


Figure 9. Coherence function between the sea surface elevation and the vertical component of the fluctuating velocity after Thornton and Kraphol: The coherence decreases in the high frequency range with depth. Adapted from Thornton and Kraphol (1974).

the surface elevation. The phase relation between the vertical and horizontal velocity similarly did not agree with the theory.

The coherence function behavior has shown very consistent results in all the studies previously mentioned. The observations point to a high coherence between the surface elevation and the vertical velocity component and a decreased value when considering the horizontal velocity component. The frequency limit for the wave related fluctuations, estimated from linear filtration, appears to be depth dependent, and a shift toward the low frequencies is observed for increasing depths. The vertical velocity component, or conversely the instantaneous sea surface elevation, are well modeled by the linear wave theory in the high energy spectral region.

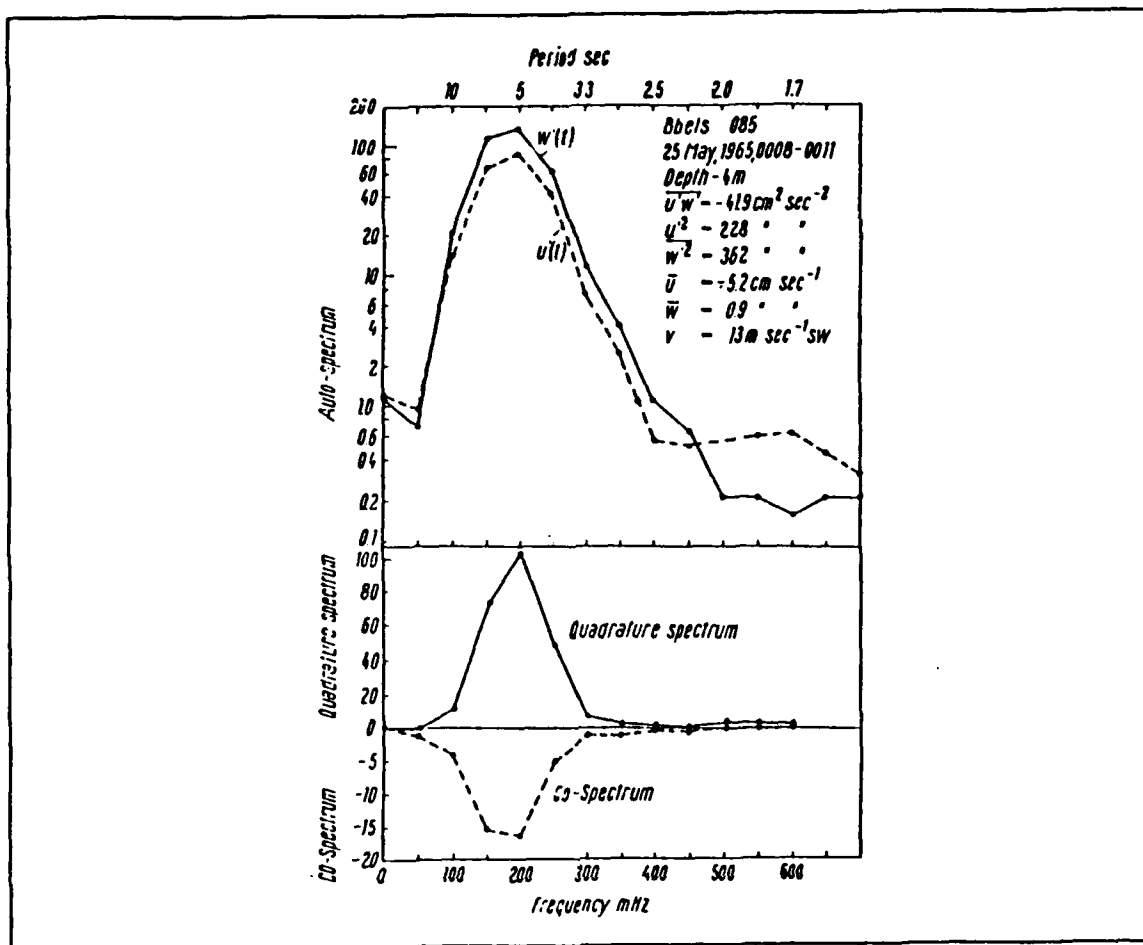


Figure 10. Spectra of the horizontal and vertical fluctuating velocity components after Shonting: The existence of a non-zero co-spectrum violates the quadrature phase relation predicted by linear wave theory for the horizontal velocity components. Adapted from Shonting (1970).

The phase studies show a different situation. Clearly different results were obtained by the different investigators. Extensive error analysis have shown no indications that could reverse the conclusions obtained. In all the studies the accurate verification of the linear theory phase relationships between the sea surface elevation and the vertical velocity component, can be noted.

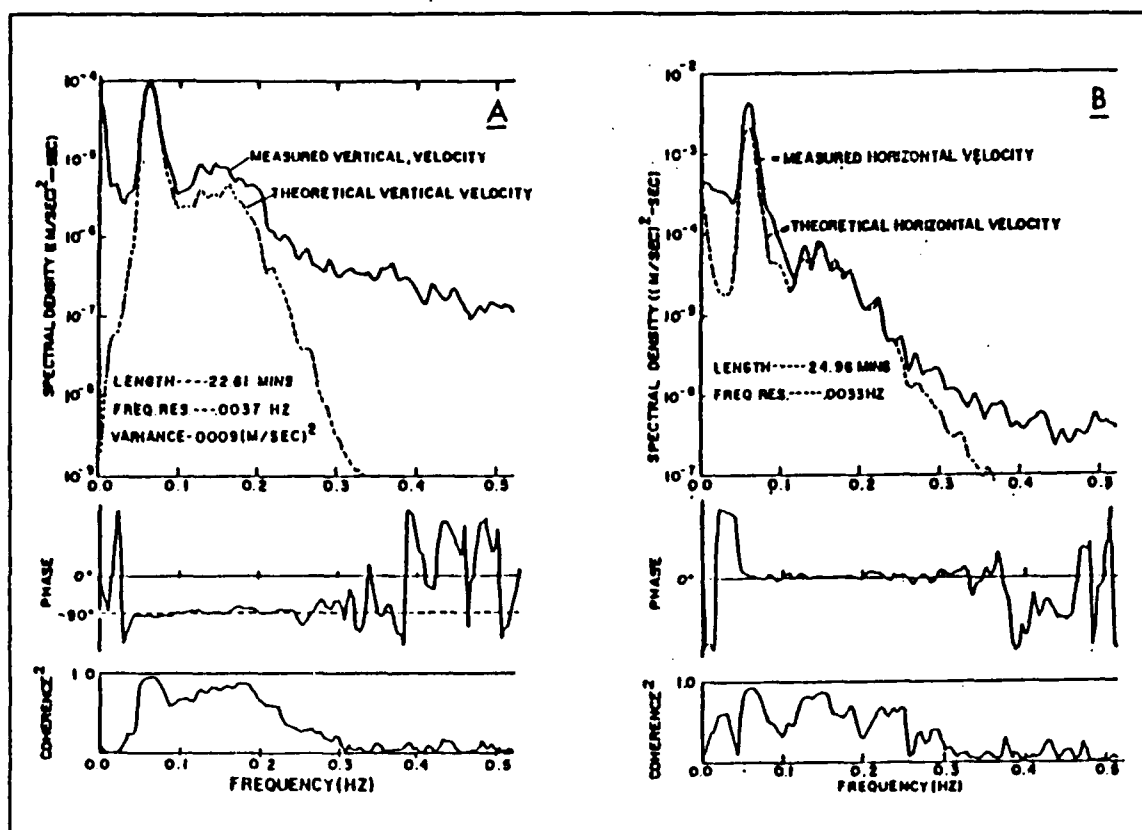


Figure 11. Phase function between the horizontal and the vertical fluctuating velocity and the sea surface elevation after Thornton and Kraphol: Measured phase relations compared well with linear wave theory for (a) the vertical velocity component of the fluctuating velocity field (quadrature) and the sea surface elevation and (b) the horizontal component of the fluctuating velocity field (in-phase) and the sea surface elevation. Adapted from Thornton and Kraphol (1974).

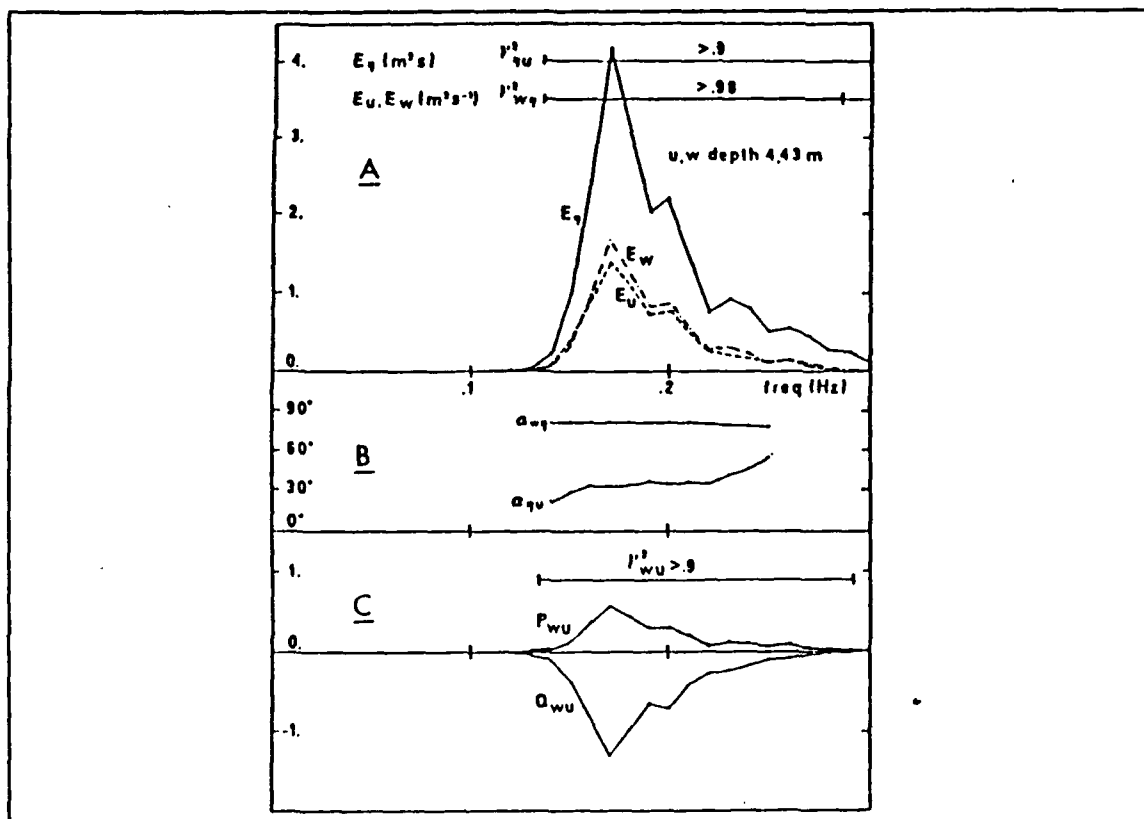


Figure 12. Phase function between the vertical and horizontal velocity components and the sea surface elevation after Cavaleri and Zecchetto: The in-phase relation for the horizontal component of the fluctuating velocity and the sea surface predicted by linear wave theory is not verified, while the vertical component of the fluctuating velocity field is in quadrature with the sea surface elevation as predicted. The sea surface elevation spectrum (E_η) and the spectrum of the vertical (w) and horizontal (u) velocity components are shown in (A). (C) shows the co (P_{wu}) and the quadrature (Q_{wu}) spectra of the vertical and horizontal velocity components. Adapted from Cavaleri and Zecchetto (1987).

III. EXPERIMENT

A. LOCATION

The SAXON (SAR and X-Band Ocean Nonlinearities) experiment was conducted from the U.S. Coast Guard Chesapeake Light Tower located on the east coast of the U.S. 14 miles offshore of Cape Henry, Virginia (see Figure 13) during the period from 14 September to 14 October 1988. The participation of the Naval Postgraduate School (NPS) was during the period from 2 to 14 October. The central goal of the experiment was to improve the understanding of the mechanisms responsible for SAR imaging of the ocean surface and upper ocean dynamics. The accomplishment of such an objective required a multi disciplinary effort, including oceanography, subsurface hydrodynamics, wave hydrodynamics, surface boundary layer mechanics and electromagnetics. The data acquired by all the participants in the experiment included

- environment conditons - wind, waves and current fields,
- wave surface feature measurements - stereophotography, video photography and wave follower,
- surface tension effects - high intensity laser, surface film sensor,
- active microwave equipment - altimeter and scaterometer, stepped-frequency delta-K radar, coherent stepped frequency CW synthetic range profile Ka-band radar, dual frequency radar, Ka-band and FM-CW scatterometer and vector slope gauge,
- passive microwave equipment - 4 dual, lineraly-polarized radiometers, and
- aircraft - real aperture radar X-band and synthetic aperture radar bands L, C and X.

Internal waves are common at this site during the period from April through October. Swells freely propagate from the open ocean as the tower location is free from wave refraction from nearby islands. The nearby bottom topography is characterized by gently sloping bottom.

The Light Tower (Figure 14) is a four-legged, 20 meters square framed structure, which housed the experiment's personnel and equipment. The diameter of each leg is about 1 meter and that of the connecting elements is 0.45 meters. The instruments described here were installed on top of a 9 meter tall bottom-mounted tower in approximately 14 meters of water. At 14 meters depth, linear wave theory predicts deep water wave conditions for waves of wavelength shorter than 28 meters corresponding to

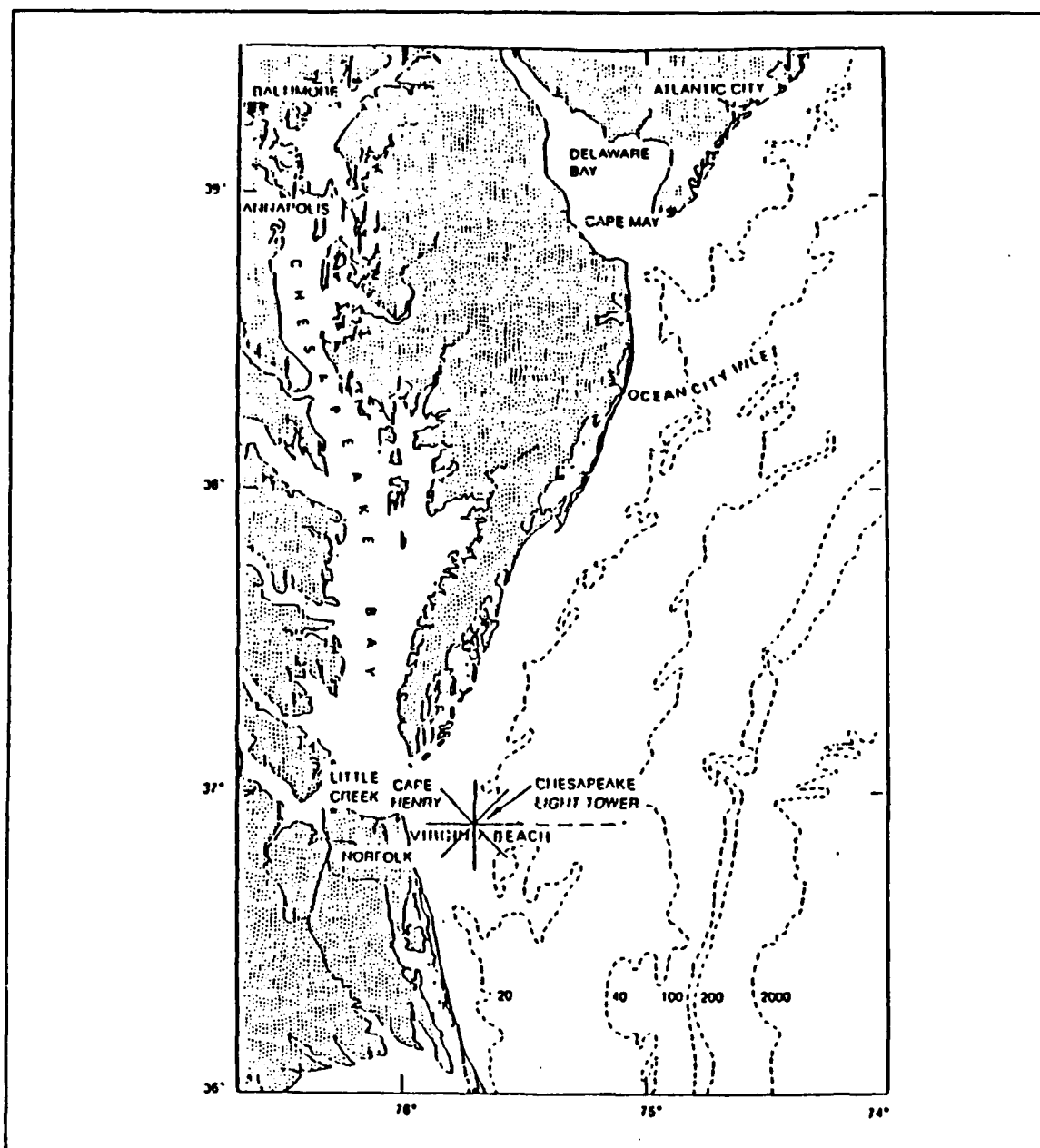


Figure 13. Location of the Chesapeake Light Tower: East coast of the United States 14 miles offshore of Cape Henry, Virginia.

periods less than 4 seconds. Shallow water conditions are observed for waves of wavelength greater than 280 meters, or periods greater than approximately 13 seconds. The instrument platform was located approximately 40 meters off the southeast side of the

main structure (Figure 14) so that the measurements are free of induced wave disturbances by the Light Tower structures for waves from the northeast to the southwest. The combined weight of the bottom mounted tower and the instrument frame was over 300 kilograms.

B. INSTRUMENTATION

The instruments deployed by the NPS, shown in Figure 15, were

- one, two component electromagnetic Marsh McBirney current meter,
- four Paroscientific quartz pressure transducers, and
- a bistatic, coherent acoustic doppler profiler which measured three components of the velocity profile above the frame (CADVP).

The characteristics of these instruments are described below.

1. Electromagnetic current meter

A Marsh McBirney model 512 OEM was used to provide a reference horizontal velocity measurement to assist with the CADVP velocity estimation. The instrument is based on Faraday's principle of magnetic induction in which a conductor, the water, moving in a magnetic field, generated within the probe, produces a voltage that is proportional to its velocity. Two orthogonal components of the water velocity field are measured in the range $\pm 3 \text{ ms}^{-1}$. The calculated error is in the band ± 3 percent with a resolution determined by the electronic noise floor. The measuring unit is a rubber covered sphere of .04 meter in diameter mounted at the end of a supporting arm of about .5 meter long and less than .01 meter in diameter. The current meter was previously calibrated.

2. Pressure transducers

Four Paroscientific series 1000 Digiquartz Intelligent Transmitters were mounted in a 2 meter square array to measure directional wave spectra. Each unit consisted of a pressure transducer and a digital interface board providing a digital pressure output. The pressure transducer has two frequency output signals, one for the pressure and the other for the internal temperature. The resolution varies according to the measurement interval. For the choice used, the manufacturer indicates a pressure resolution of 10 parts per million and a pressure integration time of 0.07 seconds. All four transducers were triggered simultaneously twice a second and then the pressure frequency counts were sequentially interrogated from each unit by a computer. The raw pressure counts and the temperature counts were converted using the manufacturer's scaling equations in the data acquisition computer. The manufacturer's cali-

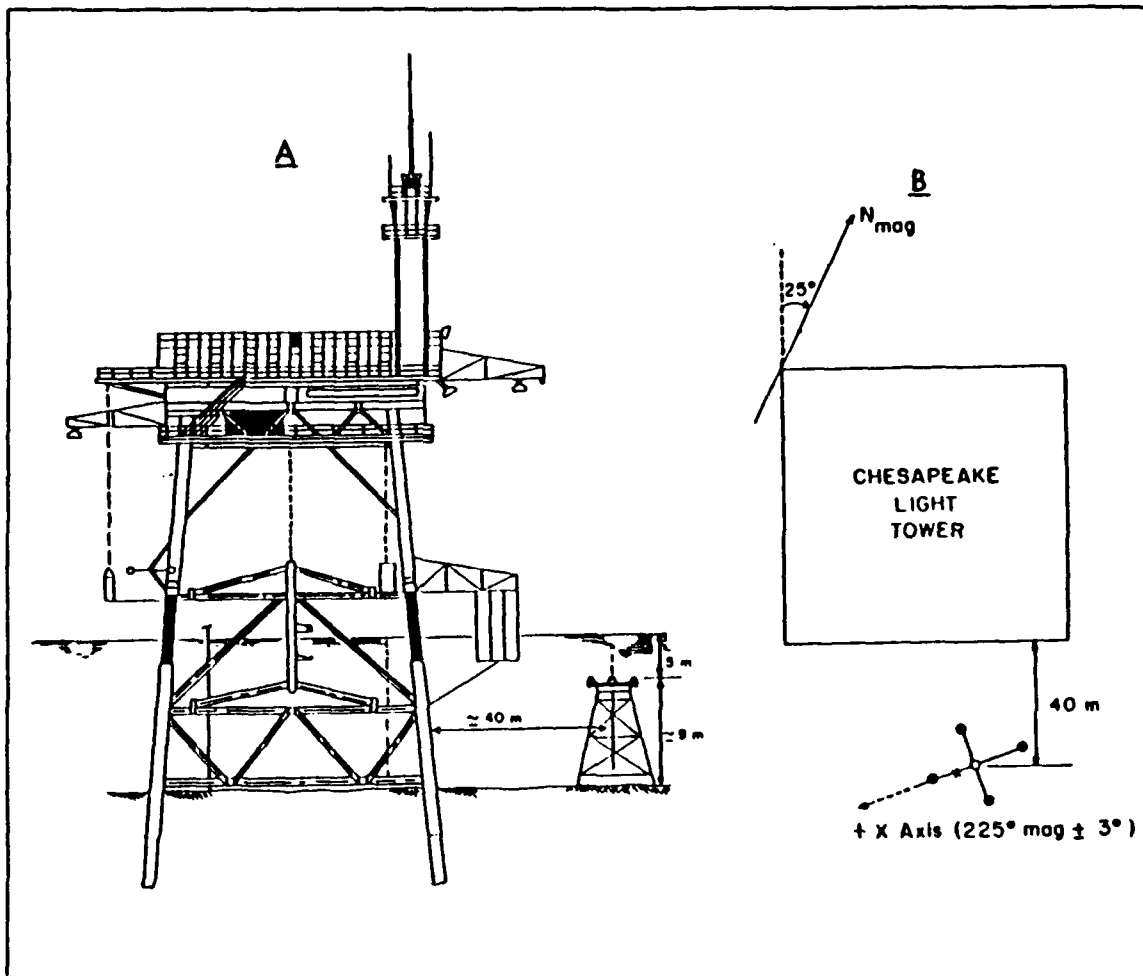


Figure 14. The Chesapeake Light Tower: (a) The structure: four-legged, 20 meters square frame. (b) Positioning of the frame of instruments relative to the tower 40 meters off the southeast corner of the tower in approximately 14 meters of water and at about 5 meters below the mean sea surface.

brations were used and a comparison with an aneroid barometer was made at the site of the experiment while the frame was in the air.

3. Bistatic acoustic doppler profiler (CADVP)

The bistatic coherent doppler profiler has a 3 degree beamwidth transducer which emits a 300 kHz sinusoidal pulse. The emitted signal ensonifies particulates and bubbles as it travels through the water column. Backscattered energy is received and

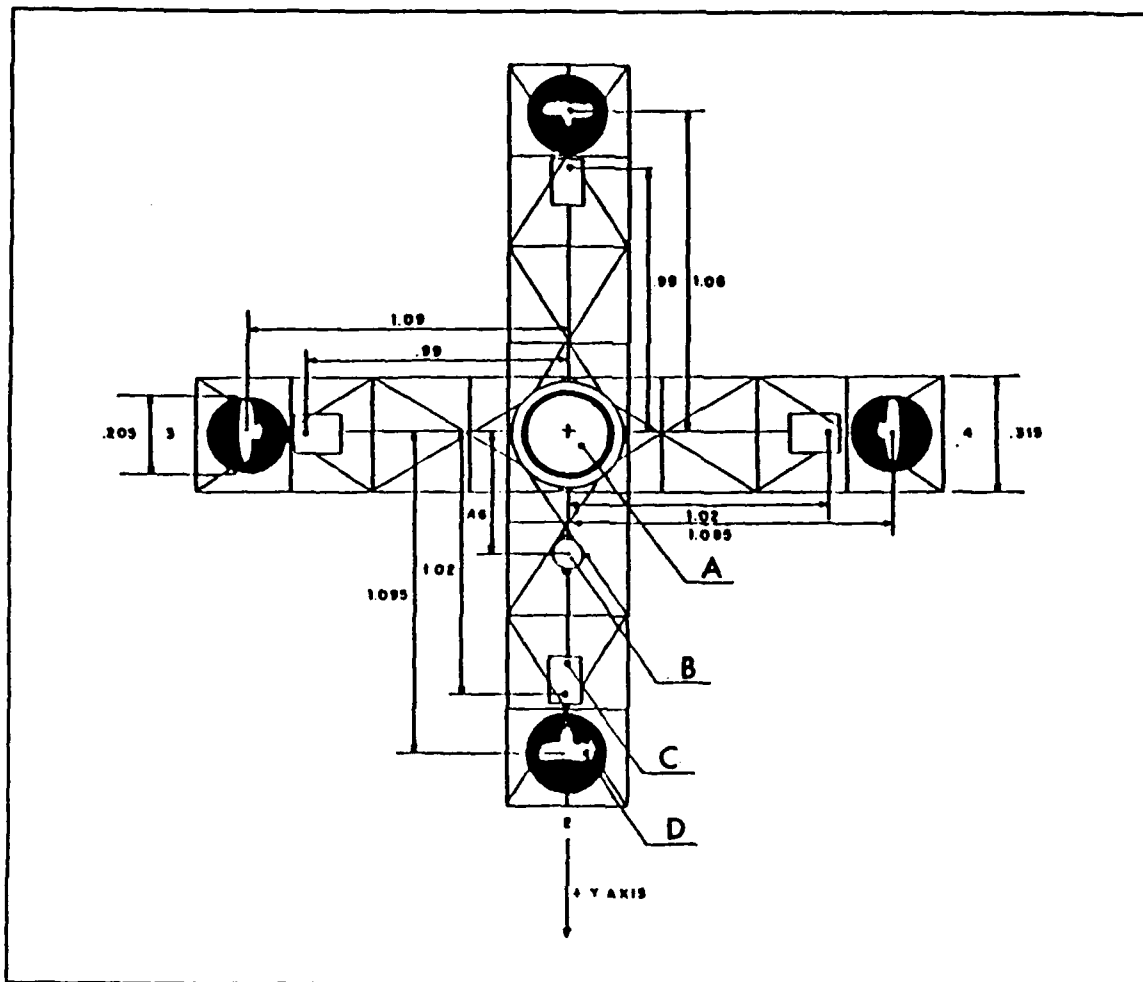


Figure 15. The frame of the instruments: A bistatic coherent acoustic doppler profiler (one transmitter (A) and four receivers (D)), one two axis electromagnetic current meter (B), and a 2 meter square slope array of four quartz pressure transducers (C). Measures are in meters.

sampled at 8 cm range intervals by the four radially placed receivers, shown in schematic configuration in Figure 15. The doppler shift between transmitted and received frequency is used to compute the velocity of the ensonified volume which is assumed to be moving with the current field.

C. DATA ACQUISITION SYSTEM

The data acquisition system used a HP310 computer to sample the electromagnetic current meter and pressure transducer, and a IIP330 computer to initialize and monitor

the CADVP system. The HP310 computer had an Infotek 16 channel, 12 bit A/D converter to digitize the electromagnetic current meter signals, and the pressure sensors were linked via a RS 232 communication loop at 19.2 Kbaud. The two channels of the electromagnetic current meter were measured with .1 ms time difference between each other and therefore have negligible time lag. The time base for sampling the current meter and pressure sensors was the computer internal clock. The data acquired with both sets of instruments was first recorded in one hour files on hard disk and later transferred to cartridge tape.

The CADVP system had a programable digitizer and sequencer which sampled the complex accoustic signals and sent the data to a digital recorder and to the HP330 computer. The time base for the data was generated by a SNAP microcomputer.

During daylight hours a video camera was used to record the image of the sea surface over the location of the bottom-mounted tower for evaluation of sea conditions and breaking events. The time code used for identification of the video images was common to the CADVP.

D. DATA

Data were acquired during 5 to 14 October 1988, and the quantities measured were:

- two orthogonal components of horizontal velocity at 4.5 meters below the surface at a sampling frequency of 8 Hz,
- four water column pressure readings at 4.5 meters depth at a sampling frequency of 2 Hz, and
- the three orthogonal components of the velocity field through the water column every 8 centimeters from 1 meter above the frame to near the surface, estimated at a 4 Hz rate.

The Massachusetts Institute of Technology (MIT) group made available to all participants 10 minute averaged meteorological data. This data set includes measurements of the wind speed and direction, air and sea temperature, and wave amplitude measured by an array of three wire gauges. The CADVP data were not used in this study, as algorithms to reliably unwrap the coherently estimated doppler shifts are still under development.

1. Processing

The velocity and pressure data were first checked and corrected for infrequent spikes by a deglitching routine. Bad data sections of up to 2 points were replaced by linearly interpolated values. Both the velocity and the pressure were corrected for the

offsets determined in the pre-experiment calibrations and an assumed atmospheric pressure of 1010 milibars was subtracted out of the pressure values.

The determination of the pressure at the central point of the array is needed in the computation of directional wave spectra, the prediction of the vertical velocity profiles as given by linear wave theory, and for comparison with the electromagnetic current meter and CADVP data. This value was calculated by using a linear interpolation of the readings of the four pressure sensors deployed. The approximation is of the form

$$P(x, y) = \frac{1}{4} (P(x^{+/-}, y) + P(x, y^{+/-})) - \frac{h^2}{4} (P_{xx}(x, y) + P_{yy}(x, y)) - \dots \quad [84]$$

where x and y are the central point coordinates, the $+$ and $-$ superscripts correspond to adding and subtracting half of the side of the square defined by the four pressure transducers to the central point coordinates, and P_{xx} and P_{yy} are second order derivatives in x and y respectively. Considering the sea surface as represented by a monochromatic wave

$$\eta(x, y) = a \cos(\vec{K} \cdot \vec{x} - \omega t) \quad [85]$$

leads to an expression for the relative error of the central point pressure approximation of the form

$$Rel. Error = \sum_{n=1}^{\infty} (-1)^{n+1} \frac{(\frac{A_l}{2})^{n+1} K^{n+1}}{2(n+1)!} \quad [86]$$

where A_l is the side of the square array, and K is the spatial wavenumber. The relative error as a function of the frequency is shown in Figure 16, when considering the first 10 terms of the series defined above. The error is less than 10 percent for frequencies smaller than .4 Hz, or waves of period greater than 2.5 seconds.

The depth of the instrument frame in the water column is required for the processing of the data and cross checking of the results. The water depth including the tidal variation was obtained by computing the mean values of the pressure records considering an averaging period of 10 minutes. Tilting of the frame relative to the horizontal is of fundamental importance for future computation of the three orthogonal components of the velocity using the CADVP data. A full period average of the four pressure

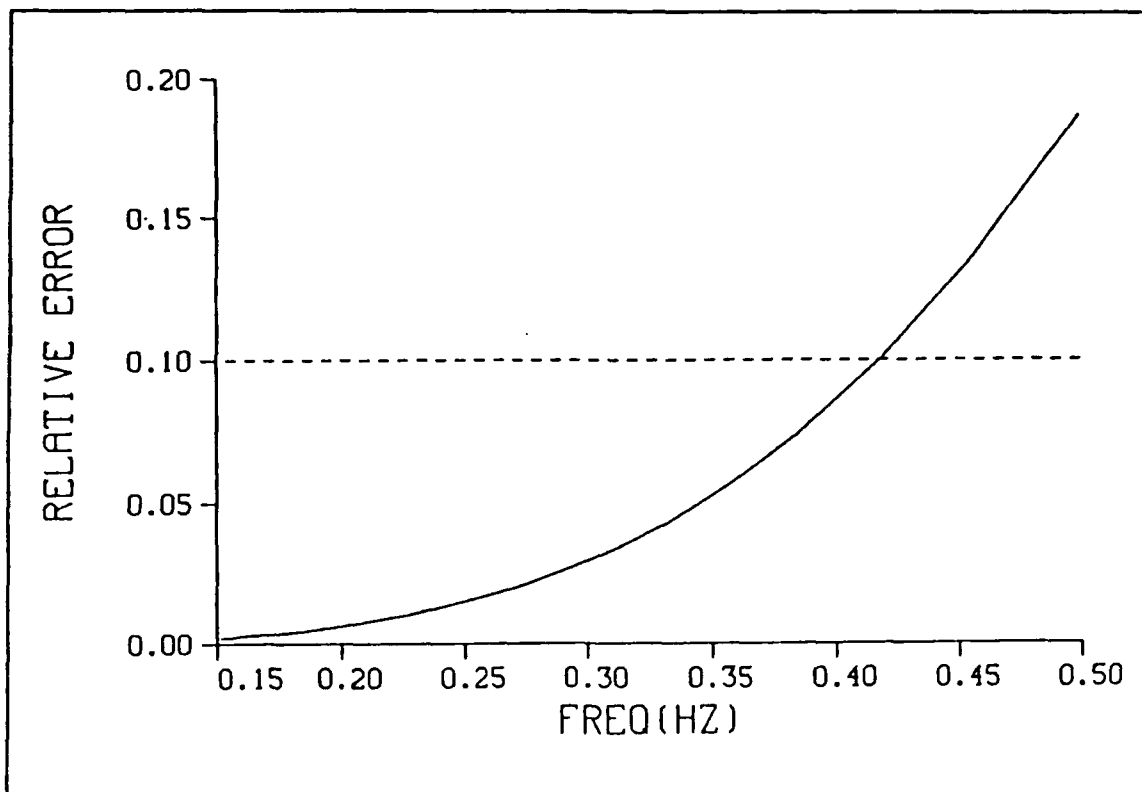


Figure 16. The central point pressure approximation: The relative error of the central point approximation versus frequency considering the first 10 terms of the approximating series ([86]) is less than 10 percent for frequencies smaller than .4 Hz.

transducers records was computed to assess this tilt. The resulting tilting of the frame was at most .28 degrees.

Mean values of the velocity components measured with the electromagnetic current meter give information on the importance of the convective processes. Averages of the two orthogonal horizontal velocity components were computed for different averaging periods.

The kinetic and potential energy of the wave field and its evolution was assessed by computing the variance of the horizontal velocity components and of the pressure records. Auto and cross spectra, phase and coherence functions of the time series were computed using the Fast Fourier Transform technique (FFT). The spectral analysis was based on one hour time series with subsampled FFT's computed over 128 second inter-

vals. The resulting ensemble averaged spectral estimate have approximately 56 degrees of freedom. The data were subjected to a trend and mean removal before being transformed, and to reduce the effects of spectral leakage, a Hamming window was used.

The computation of directional spectra was done using both the LCS and the Grauzinis methods. The Fourier coefficients of the wave field were computed using equations [42 – 46]. The Grauzinis method was implemented with the use of program TRIDEN. Three model distributions are used by this program to match the wave field Fourier coefficients, which include: the wrapped Cauchy distribution

$$D2(\theta) = \frac{1}{2\pi} \left\{ \frac{1 - m_1^2}{1 - 2m_1 \cos \theta + m_1^2} \right\} \quad [87]$$

a distribution not referred to in the statistical literature that corresponds to the analytical solution of the generating system when an exponent equal to 3 is adopted in the functional relationship of the canonical coefficients ([55]) defined by

$$D3(\theta) = \frac{1}{2\pi} \left\{ 1 + 2m_1 \frac{\cos \theta - m_1^2}{1 - 2m_1^2 \cos \theta + m_1^4} \right\} \quad [88]$$

and the wrapped Normal density distribution

$$D4(\theta) = \frac{1}{\sqrt{2\pi} \sigma} \sum_n e^{-\frac{1}{2} \frac{(\theta + 2n\pi)^2}{\sigma^2}} \quad [89]$$

where $\sigma^2 = -2 \ln m_1$. These model distributions decrease in sharpness from the wrapped-Cauchy distribution to the wrapped-Normal distribution.

The method was tested using synthetic data created by computing the Fourier coefficients of known distributions of energy. The distributions used were the box-car, tri-peak (three delta functions with amplitudes binomially distributed) and the twin-spike (two delta functions of the same amplitude). The canonical coefficients of the box-car function are defined by

$$m_k = \frac{\sin(k\varepsilon)}{k\varepsilon} \quad [90]$$

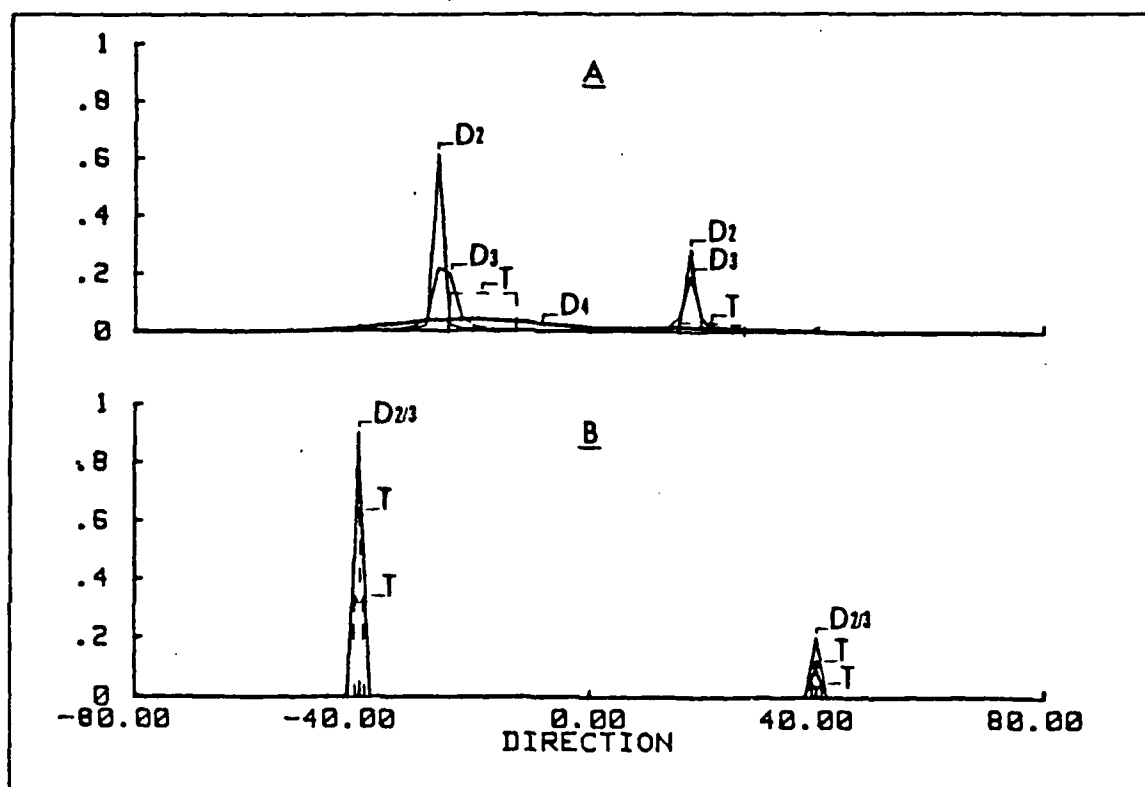


Figure 17. Testing the Grauzinis method of computing directional wave spectra: The model distributions correspond to equations [87], [88] and [89]. The test data (T) is in (A) a pair of box-car functions, and in (B) a pair of tri-peak distributions. For the broad box-car distribution the best results correspond to the least sharp model distribution D4, and for the tri-peak test data the model distribution D2 gives the best results. D4 is not represented for test (B).

where ϵ represents the width of the distribution and k the order of the coefficient. For the tri-peak distribution the canonical coefficients are formed as

$$m_k = \frac{1}{2} (1 + \cos(k\epsilon)) \quad [91]$$

where ϵ denotes the separation in direction of the side delta functions relative to the central peak. The canonical coefficients of the twin-spoke distribution are given by

$$m_k = \cos(k\epsilon) \quad [92]$$

where ϵ is half of the angular distance between the two delta functions of the distribution. A sample of the results of the tests is shown in Figure 17. Numerical results computed for some synthetic distributions are contained in Table 1. The computed directions for the energy distribution compare well with the orientation of the input synthetic data. It is noted that for broad input distributions, such as the box-car function, the sharpest model distribution gives the worse results. In fact, broad input energy distributions are matched by the separation of the uni-modal components of sharp model distributions, while for the narrow input energy distributions case the direction of the peak of energy can be achieved by rotating one of the broad uni-modal model components to the opposite direction. This last situation of sharp input energy distributions matched by broad model distributions can result in a relocation of energy in secondary directions.

The distribution adopted as representing the wave field corresponding to the data acquired during the experiment is a weighted sum of the three distributions used by the program TRIDEN. The contribution of each of the model distributions is weighted on the value of the beam separation index. In the sum, the weights are $\frac{4}{8}$, $\frac{3}{8}$ and $\frac{1}{8}$ with the largest weight corresponding to the smallest beam separation index value.

Table 1. RESULTS OF TESTS TO THE GRAUZINIS METHOD OF COMPUTING DIRECTIONAL WAVE SPECTRUM: Three synthetic distributions (DIST) were used to test the Grauzinis method of computing wave directional spectra. These distributions were the box-car (BC), tri-peak (TP) and twin-spike (TS), for different partitions of energy (ER) and orientations (DIR). These data are characterized by a LogRatio (LR) near 4. The three model distributions (D2, D3 and D4) correspond to equations [87], [88] and [89]. W represents the width of the box-car uni-modal distribution, the distance between the three delta functions of the tri-peak uni-modal distribution and the angle between the two delta functions of the twin spike distribution. The Beam Separation Index (BSI), the canonical coefficients (CNC), the directions (D1 and D2) and the percentage of energy (E1 and E2) of the model distributions are tabulated.

DIST	W	ER	DIR	LR	MD	BSI	CNC	E1	D1	E2	D2
BC	12	3:1	-20/20	4.04	D2	.012	.998	.71	-21.6	.29	18.9
					D3	.011	.997	.72	-21.3	.28	19.0
					D4	.010	.993	.75	-20.1	.25	19.9
	24	3:1	-20/20	4.05	D2	.018	.993	.64	-26.0	.36	17.8
					D3	.016	.990	.65	-25.1	.35	19.9
					D4	.011	.974	.73	-21.0	.27	19.2
TP	4	3:1	-40/40	3.50	D2	.128	.999	.75	-40.0	.25	39.8
					D3	.128	.999	.75	-40.0	.25	39.9
					D4	.128	.999	.75	-40.0	.25	40.0
	4	3:1	-20/20	4.03	D2	.011	.999	.74	-20.3	.26	19.8
					D3	.010	.999	.74	-20.2	.26	19.8
					D4	.010	.999	.75	-20.0	.25	20.0
TS	20	1:1	-20/20	4.28	D2	.137	1.	.5	-20.0	.5	20.0
					D3	.137	1.	.5	-20.0	.5	20.0
					D4	.137	1.	.5	-20.0	.5	20.0

IV. RESULTS

A. A FULL PERIOD ANALYSIS

1. Wind and Waves.

Wave power spectra, wind speed and direction and wave amplitude for the period 5 to 14 October are shown in Figure 18. The wind speed varied from negligible wind to a maximum speed of about 17 ms^{-1} . The wind blew generally from the north. Exceptions are the periods from the beginning of day 4 where the direction was highly variable to the beginning of day 7 when a full clockwise rotation of the wind direction occurred. Considering both wind speed and direction, the 10 day period can be divided into two parts. The first part (P1) was during the time of increasing wind from the north and the second part (P2), a time of variable winds.

During P1 the wind speed increased, from 4 to 17 ms^{-1} in the first three days, followed by a gradual decrease of the wind speed to values of about 1 ms^{-1} . During the entire period, the wind blew from the north, except in the final half day when the winds were light and had variable direction. This evolution is clearly seen in the representation of the wave power spectra (Figure 18). In the beginning of P1, the peak wave energy was observed at 10 seconds period. When the wind started blowing with increased speed, the peak period of the waves shifted to 5 seconds. A gradual evolution was then observed with increasing wave periods to about 16 seconds when the wind started decreasing. This shift of the peak of wave energy is consistent with the classic wave model evolution for winds of increasing speed. The rms wave amplitude plot (Figure 18) shows progressively growing waves, from an initial amplitude of .5 meters to amplitudes of about .9 meters. It is also noted there was delay of the wave field to the increase of the wind speed, and a slower rate of decrease of the wave amplitude when the wind began to slow down.

P2 was highly variable in wind speed and direction. An increase of the wind speed from 5 to 14 ms^{-1} during day 6 while progressively changing direction resulted in a weak signature in the wave power spectra and wave amplitude (Figure 18). The increase of the wind speed during days 7 and 8 accompanied by a steady direction is reflected in wave spectra with peak of 5 seconds period. However the evolution of the long period wave field did not parallel the P1 period.

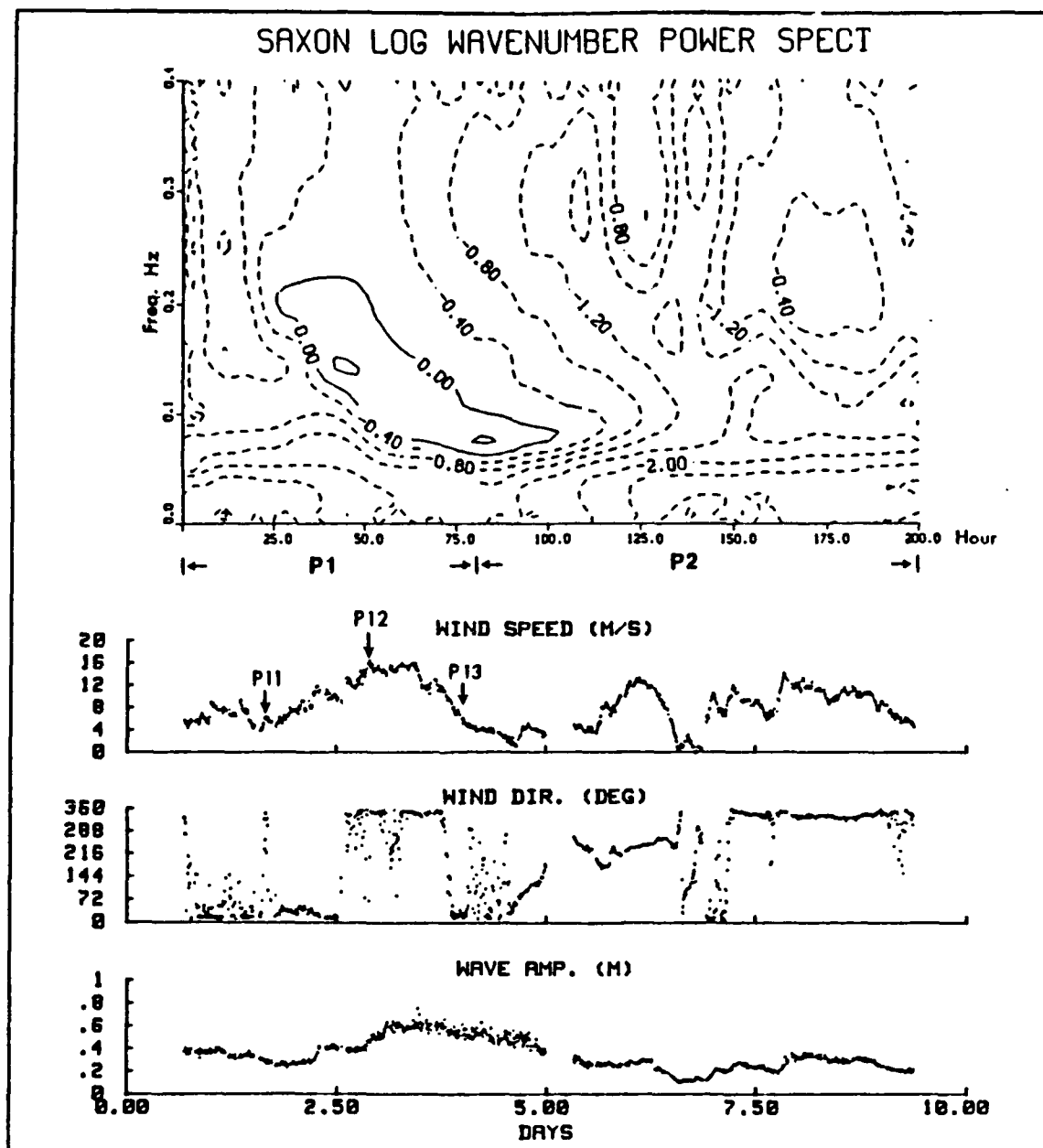


Figure 18. 5 to 14 October wave and wind fields summary: Wave power spectra computed from the pressure data. Wind speed and direction, and wave amplitude (MIT) are 10 minute averages. Day 0 corresponds to 5 October at 00:00:00.

2. Horizontal velocity

Ten minute averaged time series of means and variances of the velocity data measured with the electromagnetic current meter and also the time series of the mean wind speed and direction are shown in Figure 19. The u component of the mean horizontal velocity clearly shows the influence of the tidal currents. This result could be expected from the current meter orientation, where the positive x axis pointed towards the entrance of the Chesapeake Bay. The mean value of the u component varied from approximately -20 to 10 cm s^{-1} . During P2, a 360 degrees rotation of the wind direction, and an increased value of the u component of the horizontal velocity is noticed. This is particularly true when the wind was blowing from the west. The mean v component had a completely different behavior. Its values range from 0 to -30 cm s^{-1} , and its evolution closely follows the wind field. No tidal signature is apparent. The variances of both components had a very similar behavior to the wave amplitude time series (Figure 18). It can be noticed that there was considerably greater variance associated with the v component of the horizontal velocity, particularly during P1. In this period the values of the variance for the u component range from 30 to 180 cm^2s^{-2} while the v variance varied from 20 to 300 cm^2s^{-2} .

3. Air and sea temperature

The evolution of the air and sea temperature from 5 to 14 October is shown in Figure 20. During almost all the period, there was an unstable boundary layer situation with the air colder than the water. An exception is day 7. During all the period, the sea temperature decreased continuously with values ranging from 18 to 21 degrees centigrade. The air temperature oscillated between 9 and 21 degrees. The unstable situation associated with the active wind conditions resulted in a well mixed water column. As a result internal waves were not observed.

B. SELECTED PERIOD ANALYSIS

Three, one hour periods were selected for detailed analysis during P1

- 6 October from 16:10 to 17:10 (P11),
- 8 October from 8:40 to 9:40 (P12), and
- 9 October from 6:40 to 7:40 (P13)

which are indicated on the wind speed time series (Figure 18). The results for each of these one hour periods include:

- directional wave spectra computed by the Grauzinis method and by the LCS method (only the results for day 6 are shown for LCS),

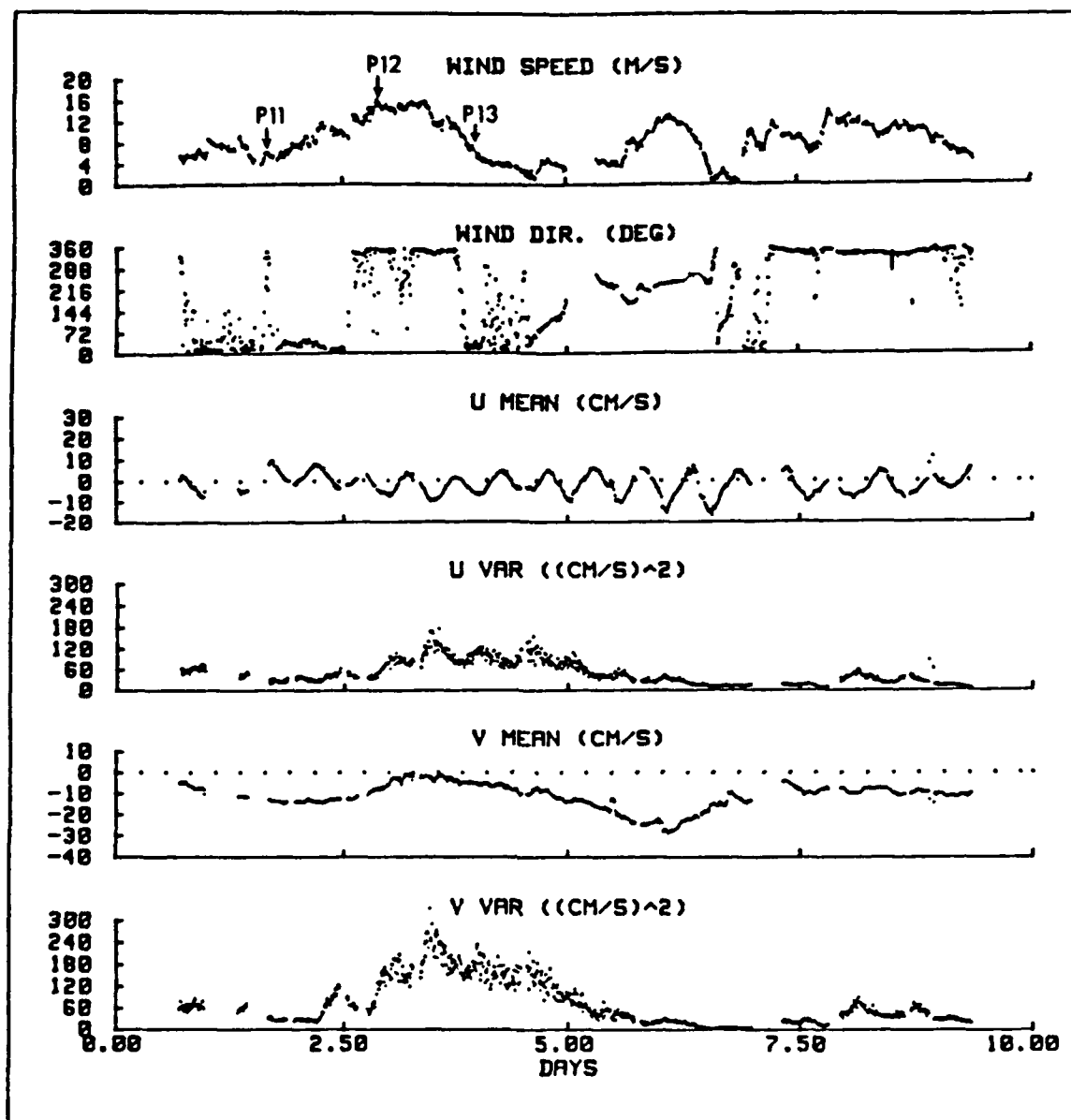


Figure 19. 5 to 14 October horizontal velocity summary: Means and variances of the two orthogonal components of the horizontal velocity measured with the electromagnetic current meter. The averaging period is 10 minutes. The wind speed and direction are also represented.

- directional information as obtained from the two orthogonal components of the horizontal velocity (only the results for 6 October are shown),
- spectral density functions of the two orthogonal horizontal velocity components,

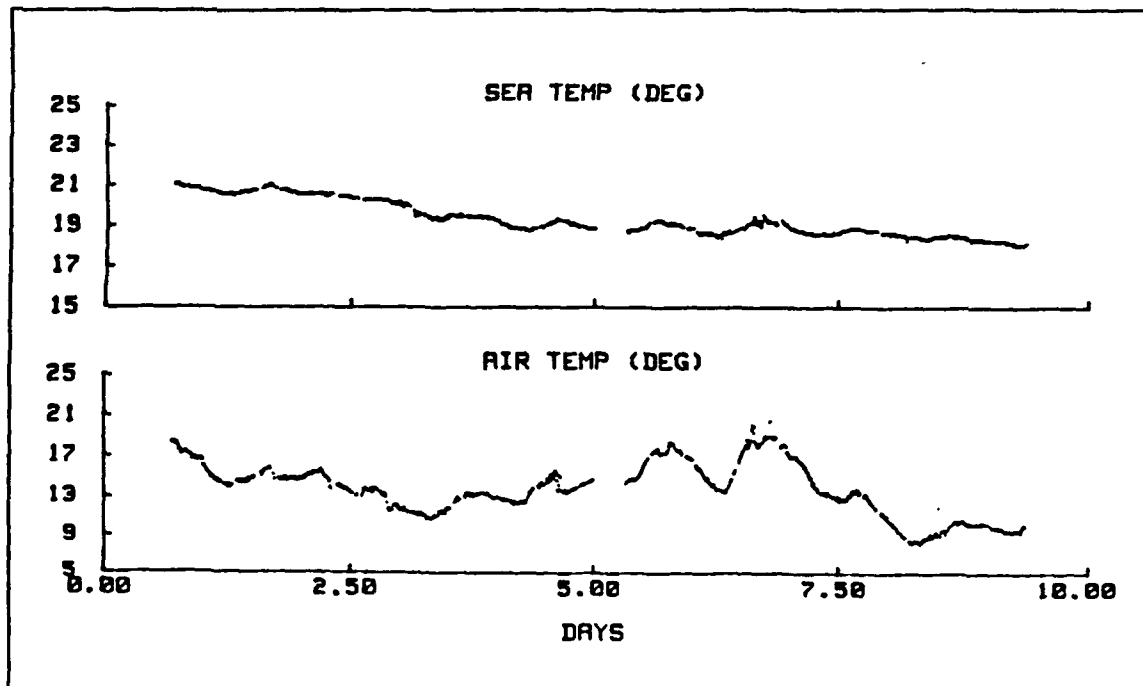


Figure 20. 5 to 14 October air and sea temperatures summary: Ten minute averages of the air and sea temperature show the atmosphere colder than the water which is characteristic of an unstable boundary layer situation.

- phase and coherence functions between each of the horizontal velocity components and the sea surface elevation computed from the pressure data, and
- sea surface elevation spectral density functions computed from the pressure and horizontal velocity measurements.

1. P11

The first one hour period corresponds to the beginning of the increasing wind speed. The direction of the winds was variable, ranging from the north-northwest to the southeast. The mean wind speed was 6 ms^{-1} . The significant wave height for the period was 1 meter and the peak period of the wave field was 9.8 seconds (frequency .1 Hz). The mean u component velocity was 3 cms^{-1} and the v component -12 cms^{-1} , and the tide was at high water.

The directional wave spectrum computed by the exact Fourier coefficients representation method is shown in Figure 21 and Figure 22, and the directional wave spectrum computed by the LCS method in Figure 23. The directional spectrum com-

puted by the first of the two methods shows a range of directions in the high energy region of the spectrum (.06 to .2 Hz), from the east-northeast to the south-southeast. Two distinct peaks of energy can be observed. The first in the frequency range from .08 Hz to .12 Hz (swell) with a mean direction of east, and the second in the frequency range .15 to .2 Hz (sea) with a mean direction of east-northeast. An annulus of energy can be observed in almost all directions in the band of frequencies of significant energy. The results obtained by the LCS method are, at first impression, different. Careful observation shows that the difference is solely in the direction pointed by the center of the main lobe. The LCS results in a much smaller directional resolution, typically greater than forty degrees, and the range of directions encompassed by the directional lobe includes, in this case, for each frequency the results obtained for the directional spectrum computed by the exact Fourier coefficients representation method. The LCS method shows the previously mentioned negative side lobes of the model distribution of energy. Mean directional information computed from the horizontal velocity components (Figure 24) compare well with the results of the exact Fourier coefficients representation method.

The spectral density functions of the two orthogonal horizontal velocity components, coherence and phase functions between the u and v components of the horizontal velocity and the sea surface elevation and the spectral density function of the sea surface elevation are shown in Figure 25. The spectral density function of the velocity components shows an energy peak at about .1 Hz which agrees with the peak of the sea surface elevation. The v component of the horizontal velocity has a higher level of energy than the u component. Recalling the results of the directional wave spectrum and the electromagnetic current meter orientation, positive v points toward the southeast, showing that the increased level of energy for the v component is related to the wave field direction. The coherence function is different for the two velocity components. The level of coherence is greater for the v component with values of .8 for the high energy frequency range. The coherence values are about .6 for the u component in the corresponding frequency range. The phase function shows both components of the horizontal velocity in-phase with the sea surface elevation, a result expected from the linear wave theory. The spectral density function observed with the slope array and predicted from the velocity data compare well. In the high energy frequency range the plot of the sea surface elevation spectral density function shows a greater potential energy.

2. P12

The second one hour period, 8 October from 8:40 to 9:40, corresponds to the end of the increasing winds. During this period, the winds blew from the north with a

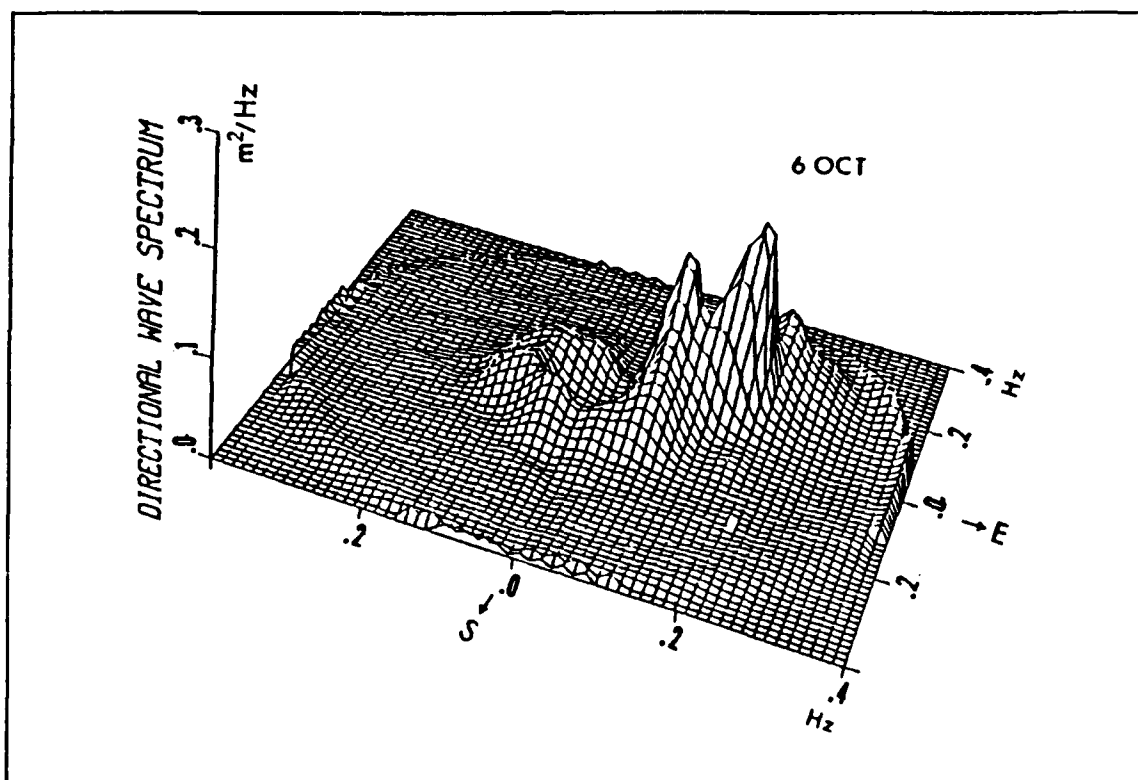


Figure 21. Directional wave spectrum for 6 October 16:00 to 17:00 computed by the Grauzinis method (3D representation): Two distinct peaks of energy can be observed. The first in the frequency range .08 Hz to .12 Hz (swell) and the second in the band of frequency .15 to .2 Hz (sea).

mean speed of 15 ms^{-1} . The peak period of the wave field was 7.5 seconds (.13 Hz) and the significative wave height was 2.3 meters. The mean horizontal velocity (u,v) components were -2 cms^{-1} and -6 cms^{-1} . The tide was half way between the high and low tide.

The directional wave spectrum computed by the Grauzinis method is shown in Figure 26 and Figure 27. The spectrum is narrower than in the previous one hour period, and the variance has increased. The waves associated with the peak of energy are coming from the east. As frequency increases, there is a rotation in the direction of the wave field towards the north. In the range of significant energy, the spectrum spreads from the east to the northeast. The directional spectrum computed by the LCS method (not shown) had as in the previous one hour period a different principal direction for the main lobe of the model distribution, but as before the direction obtained with the

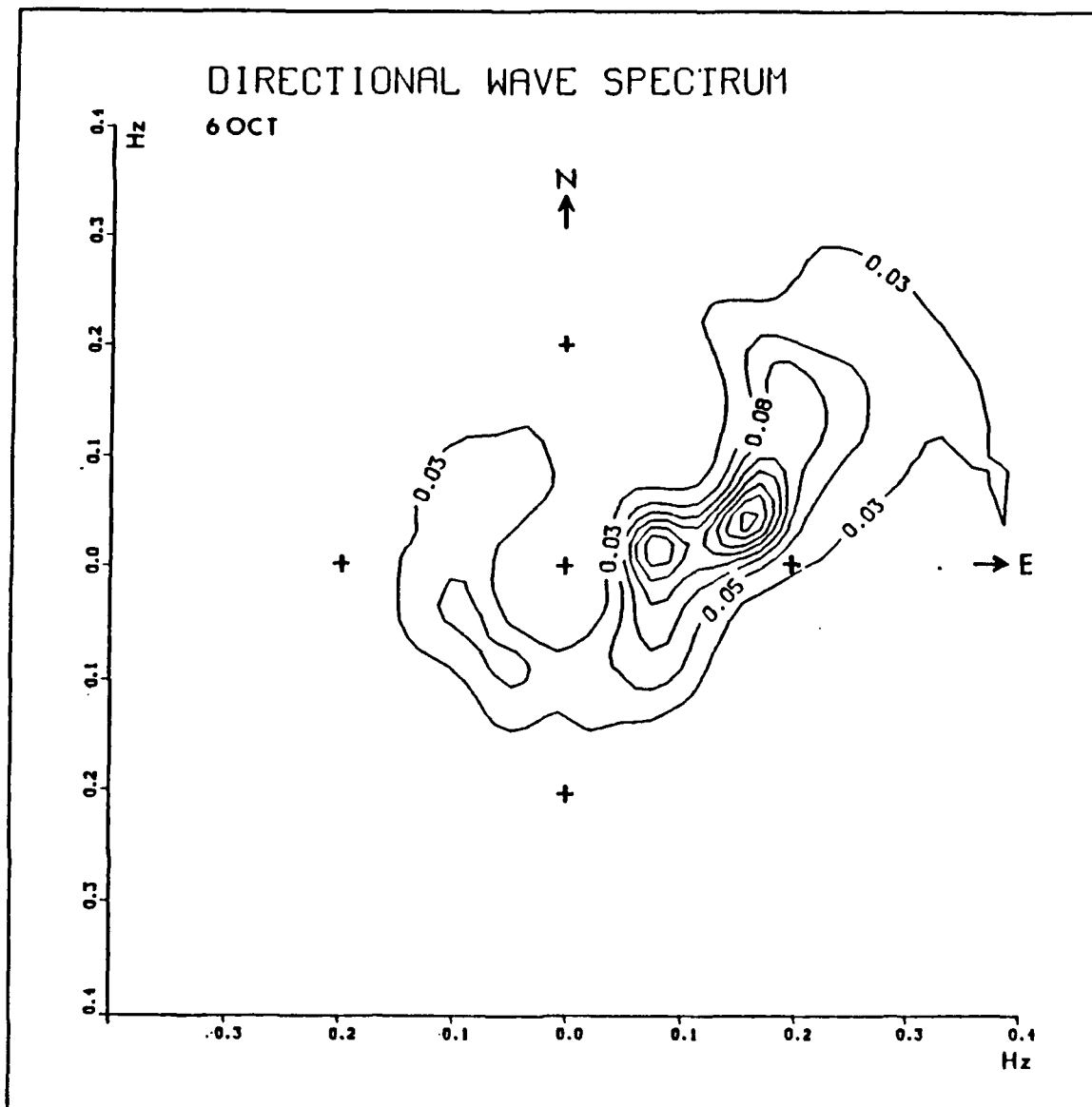


Figure 22. Directional wave spectrum for 6 October 16:00 to 17:00 computed by the Grauzinis method (top view): As in the 3D representation an annulus of energy in the high energy frequency band can be noticed. The radial distance corresponds to frequency and the orientation of the plot is as specified (north on top).

Grauzinis method was inside the main lobe. The directional information from the electromagnetic current meter data (not shown) was in close agreement with the results

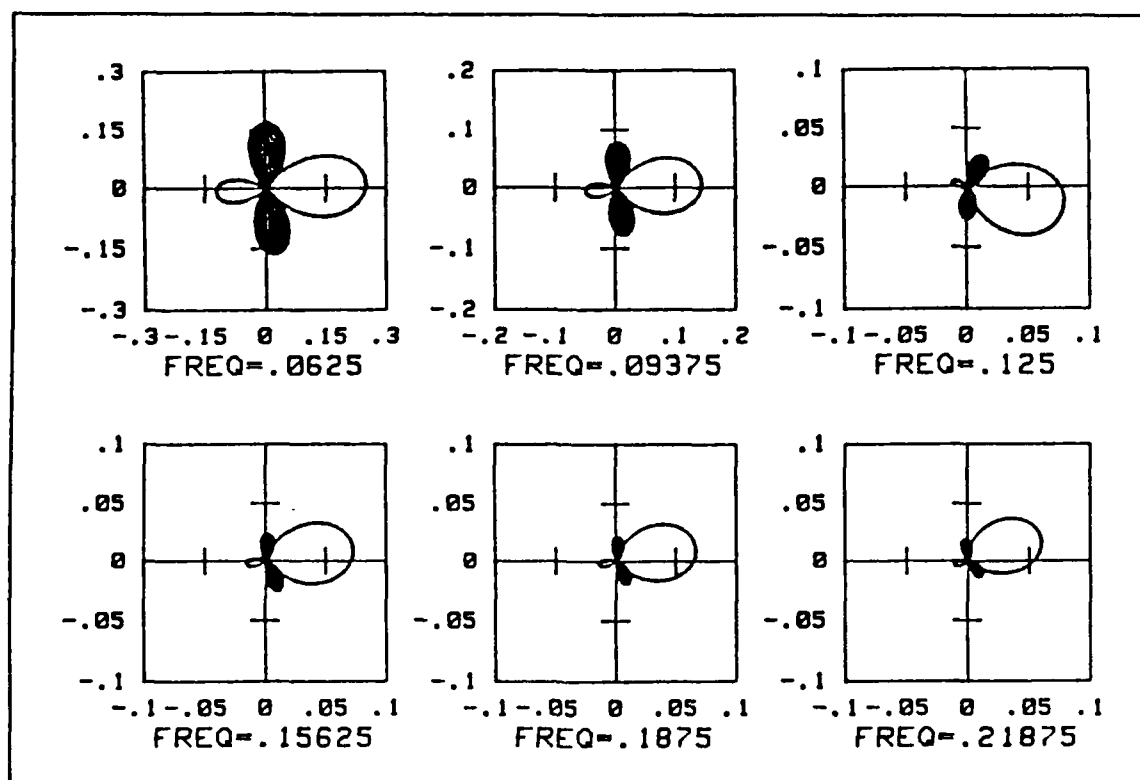


Figure 23. Directional wave spectrum for 6 October 16:00 to 17:00 computed by the LCS method: Shaded areas represent the negative side lobes of the model distribution, which is a characteristic of the method. Increased negative side lobes correspond to frequencies containing less energy. The directional lobes contain the range of directions computed by the Grauzinis method.

of the Grauzinis method. During this period, notice that the annulus of energy previously spread over almost all directions is reduced.

The summary of the spectral quantities computed for the velocity and sea surface elevation is shown in Figure 28. Comparing the spectral density functions, the v component of the horizontal velocity shows greater levels of energy than the u component. The v component spectrum has a main peak of energy at .13 Hz (7.7 seconds) and a secondary peak of energy at about .18 Hz (5.6 seconds) that can be also observed in the sea surface elevation spectral density function computed from the slope array data. The coherence function between the v component and the sea surface elevation shows

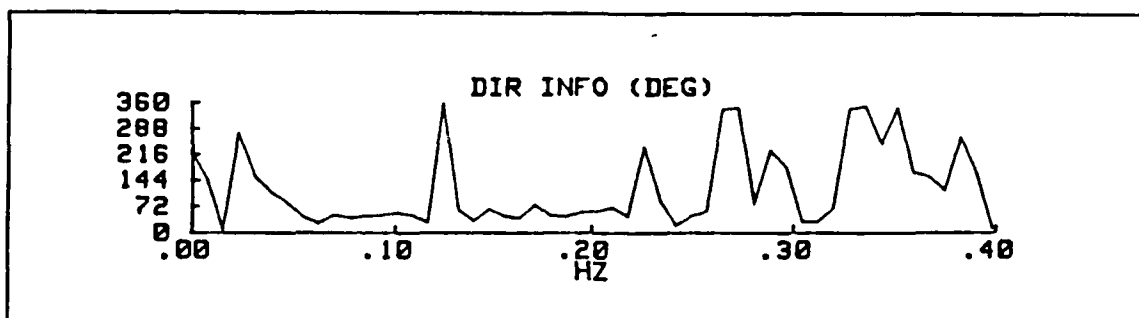


Figure 24. Directional information for 6 October 16:00 to 17:00: Computed from the two orthogonal components of the horizontal velocity. This information compares well with the results computed using the Grauzinis method.

high values, .95, in the range of frequencies from .8 to .23 Hz, that is in the range of high energy. Lower levels of coherence between the sea surface elevation and the u component are observed, with maximum values of .65 in the range of high energy. The phase function shows the u and v components of the horizontal velocity in phase with the sea surface elevation. Good agreement is observed between the spectral density function of the sea surface elevation computed from the pressure data and the horizontal velocity. Contrary to the previous period, there is a greater level of kinetic energy. It is recalled that this period was characterized by high wind speeds and increased significant wave height.

3. P13

The last selected one hour period, 9 October from 6:40 to 7:40, corresponds to the light winds region of P1. The observed mean wind speed was 4 ms^{-1} blowing steady from the north-northeast. The computed significant wave height was 1.9 meters and the peak period of the wave field 12.8 seconds (.08 Hz). The mean velocity components had values of 4 cms^{-1} for the u component and -5 cms^{-1} for the v component. The tide was high water.

The directional wave spectra computed by the Grauzinis method is shown in Figure 29 and Figure 30. The range of directions is the narrowest of the three selected one hour periods. The direction of the peak frequency is from the east. The directional spectrum computed by the LCS method (not shown) had as before a different direction of the main lobe. As in the first one hour period, there is an annulus of energy spread over almost all the directions. The directional information computed from the horizontal

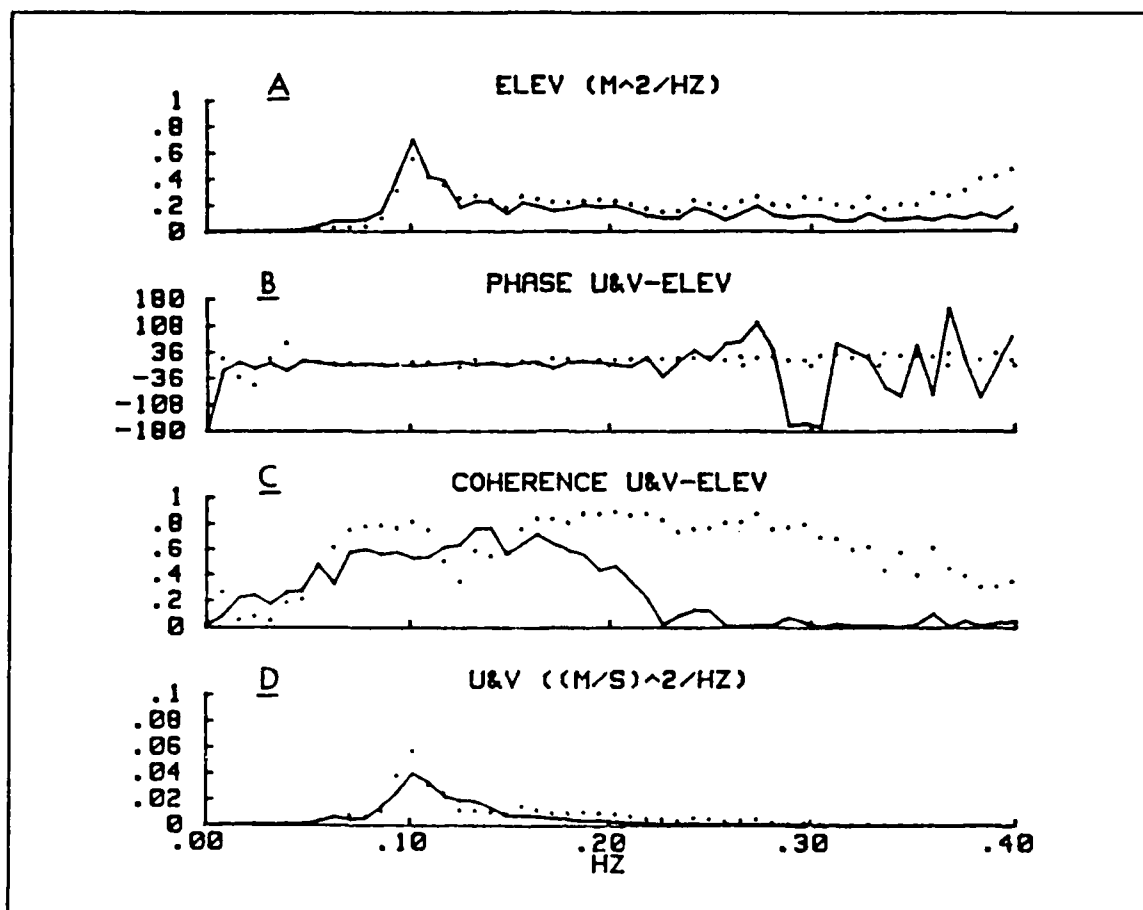


Figure 25. Spectral functions of the sea surface elevation and horizontal velocity components for 6 October 16:00 to 17:00: (A) Spectral density function of the sea surface elevation computed from the pressure data (solid line) and from the horizontal velocity (dotted line). The two spectra compare well. (B) Phase spectra between the horizontal velocity components and the sea surface elevation. An in-phase relation as predicted by linear wave theory is observed (u solid line and v dotted line). (C) Coherence spectra between the horizontal velocity components and the sea surface elevation. Higher coherence for the v component (dotted line) is observed. (D) Spectral density of the two orthogonal components of the horizontal velocity (u solid line and v dotted line).

components of the velocity (not shown) compared well with the results of the directional spectrum computed by the Grauzinis method.

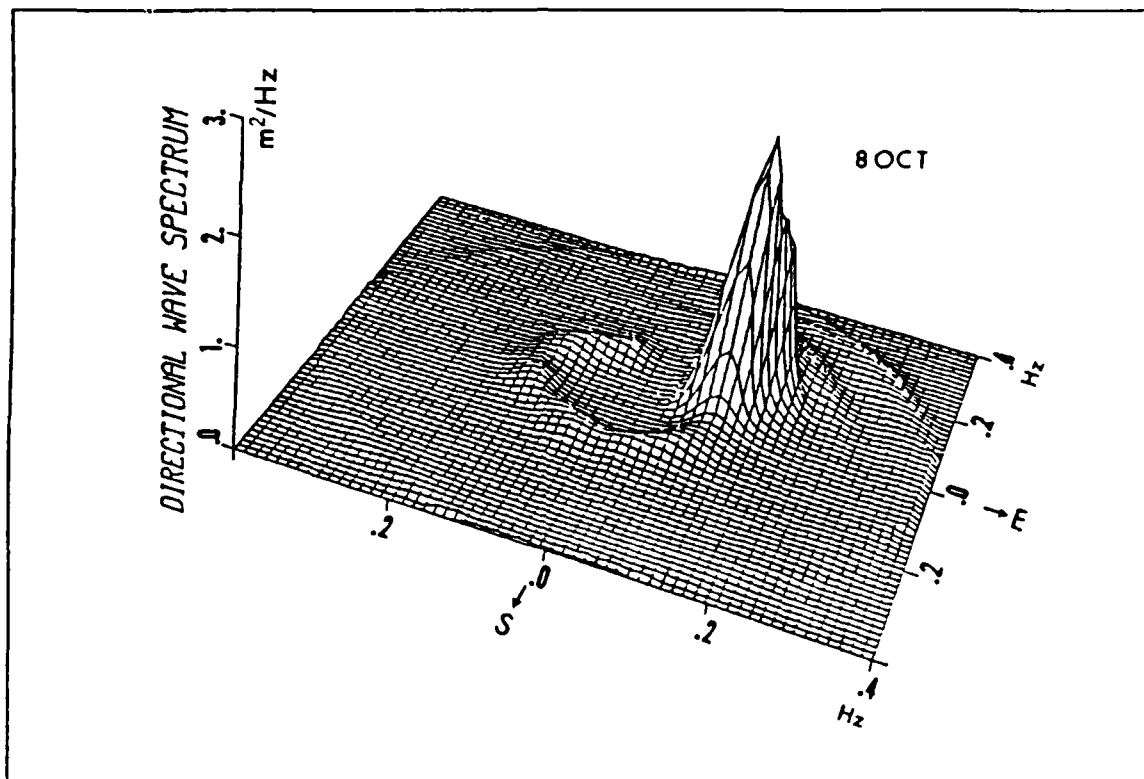


Figure 26. Directional wave spectrum for 8 October 8:40 to 9:40 computed by the Grauzinis method (3D representation): A narrower spectrum than in P11 is observed. Only one peak of energy at .13hz (7.5 seconds). The annulus of energy is smaller than in the one hour period of 6 October (Figure 21).

A summary of the spectral quantities of the velocity components and sea surface elevation is shown in Figure 31. The spectral density functions of the horizontal velocity components show a greater level of energy for the v component. Contrary to the previous one hour period the peak of energy for the two horizontal velocity components is now different. The energy peak of the v component agrees with the peak of the spectral density function of the sea surface elevation computed from the slope array measured pressures. The coherence functions between the horizontal velocity components and the sea surface elevation show a reduced value for the u component of the velocity with a maximum of .47. The phase relations as before show the u and v components of the horizontal velocity in phase with the sea surface elevation. The sea surface elevation

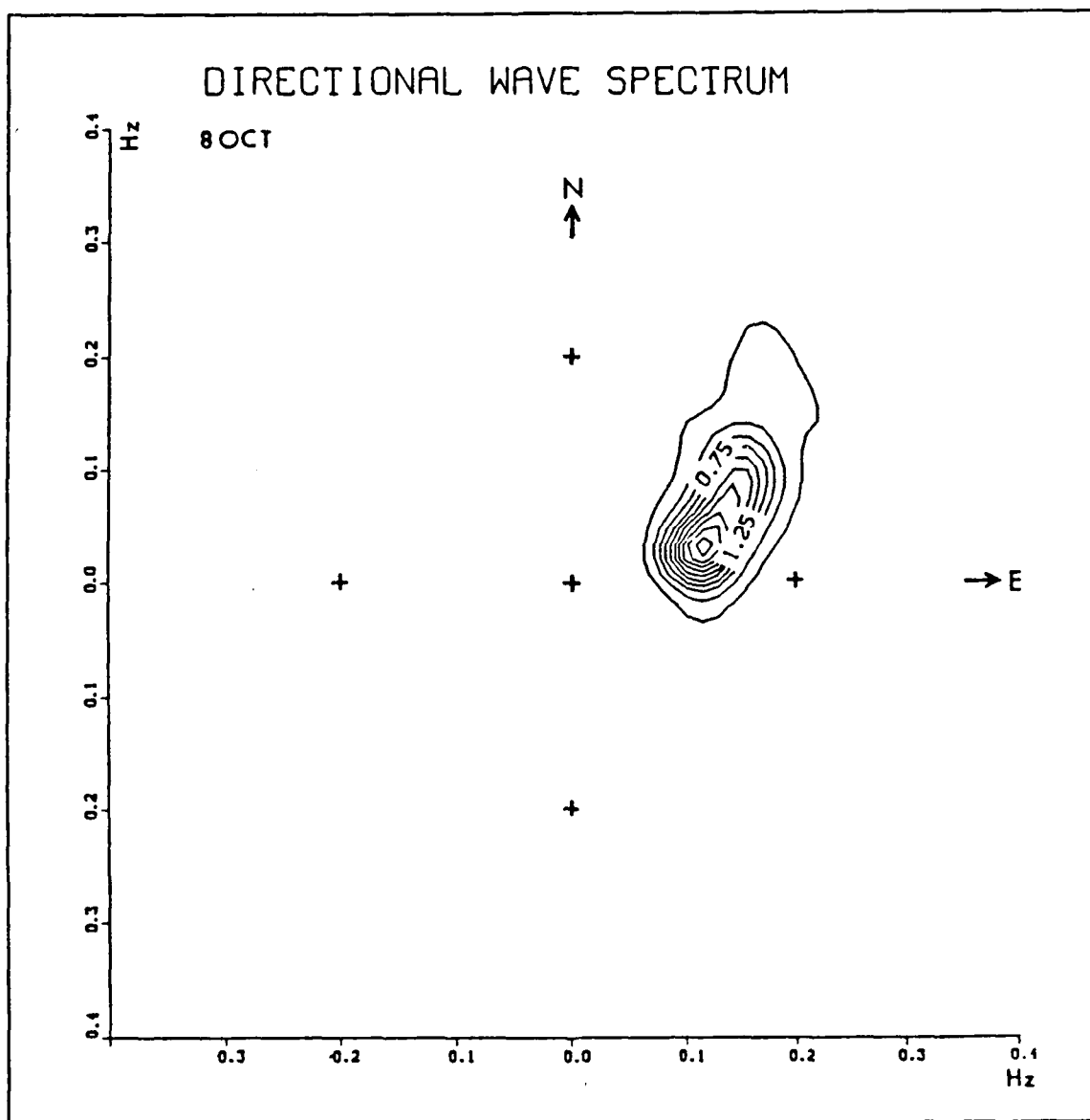


Figure 27. Directional wave spectrum for 8 October 8:40 to 9:40 computed by the Grauzinis method (top view): A narrower range of frequencies and directions than for the one hour period of 6 October. Radial distance corresponds to frequency and the orientation of the plot is as specified (north on top).

spectral density function computed from the pressure and from the velocity data do not show as good agreement as for the other two one hour periods.

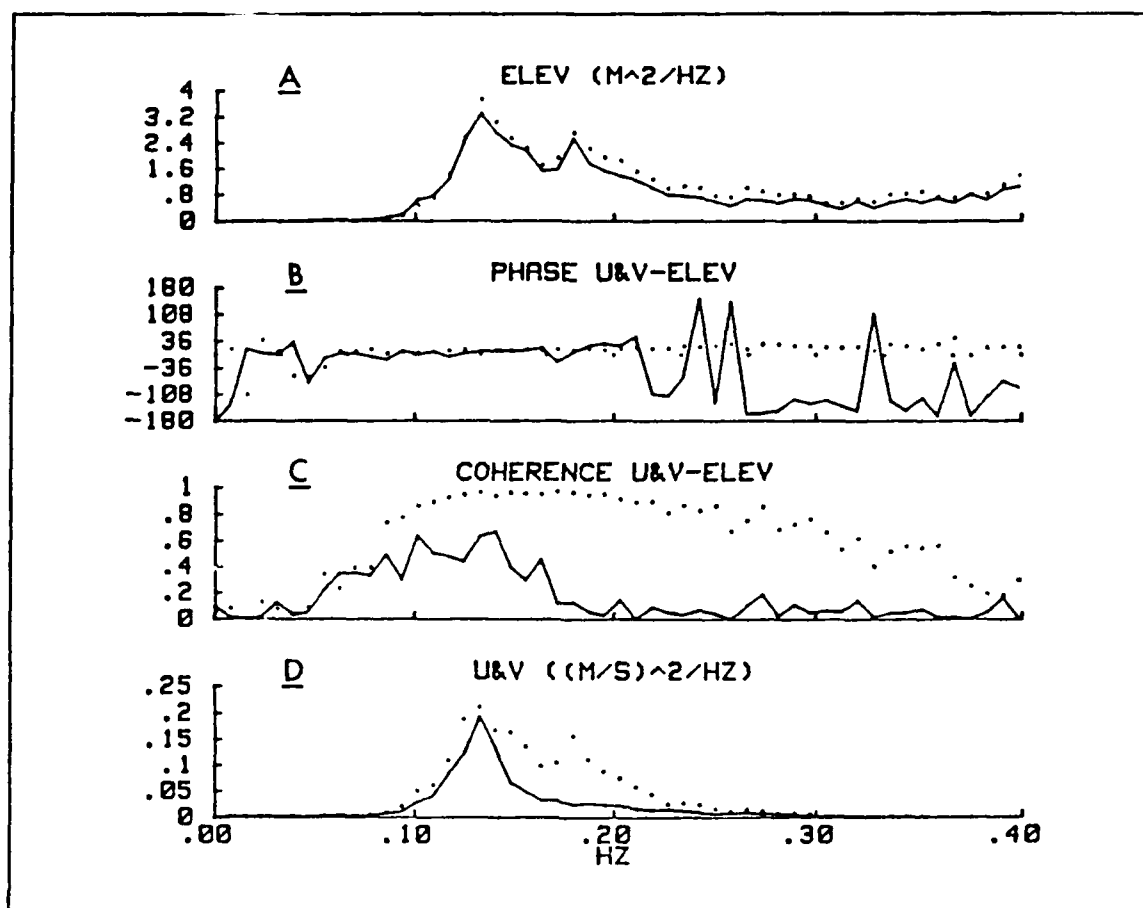


Figure 28. Spectral functions of the sea surface elevation and horizontal velocity components for 8 October 8:40 to 9:40: (A) Spectral density function of the sea surface elevation computed from the pressure data (solid line) and from the horizontal velocity (dotted line). The two spectra compare well. (B) Phase spectra between the horizontal velocity components and the sea surface elevation. An in-phase relation as predicted by linear wave theory is observed (u solid line and v dotted line). (C) Coherence spectra between the horizontal velocity components and the sea surface elevation. The u component (solid line) shows a much smaller coherence with the sea surface elevation than the v component (dotted line). (D) Spectral density of the two orthogonal components of the horizontal velocity (u solid line and v dotted line). More energy is observed for the v component of the horizontal velocity.

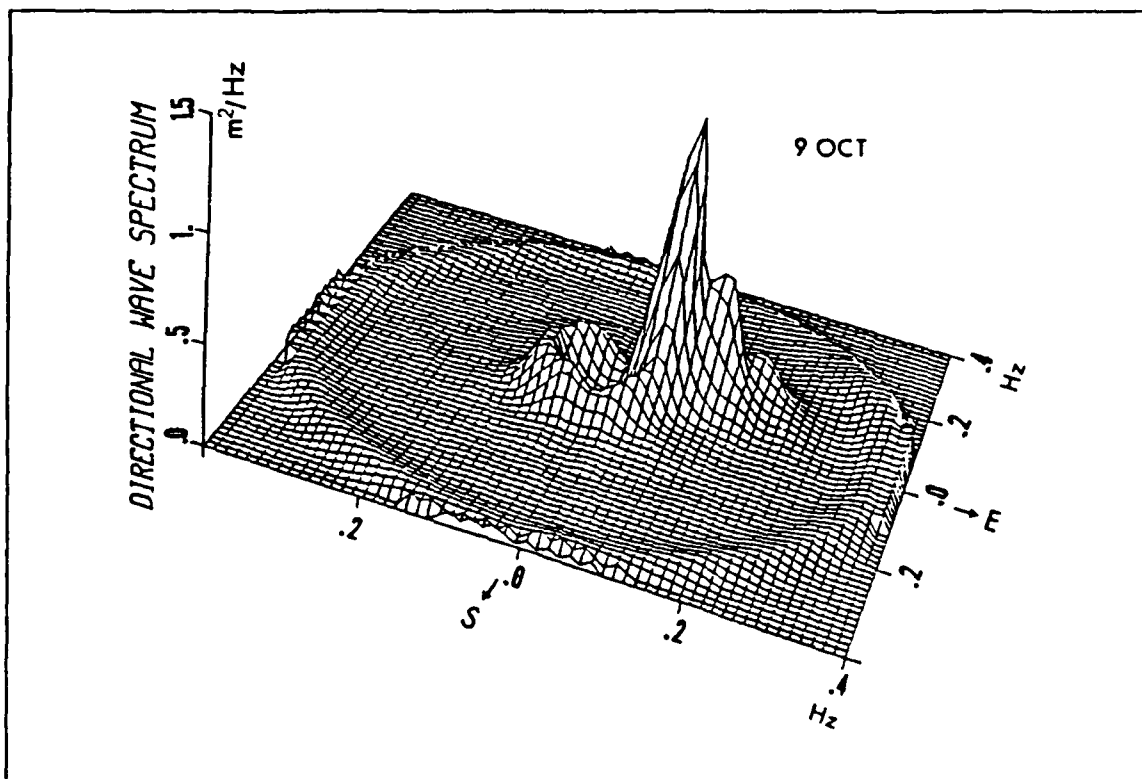


Figure 29. Directional wave spectrum for 9 October 6:40 to 7:40 computed by the Grauzinis method (3D representation): A principal (.08 Hz) and a secondary peak of energy are observed. An annulus of energy spread over almost all directions, in the frequency band of high energy, is seen.

C. DISCUSSION

1. Directional wave spectrum

The computation of the directional wave spectrum with the exact Fourier coefficients representation method have shown results in good agreement with the equivalent information computed by different methods. The model distribution chosen to represent the bivariate wave spectrum, a weighted sum of the three model distributions used by program TRIDEN, reflects the weakness of the available indicators for the best fitting distribution. The analysis showed an annulus of energy spread over almost all directions in the frequency range of significant energy. For very sharp distributions of energy and if the uni-modal model distributions are too broad, the matching of the input Fourier coefficients is done by moving one of the components away from

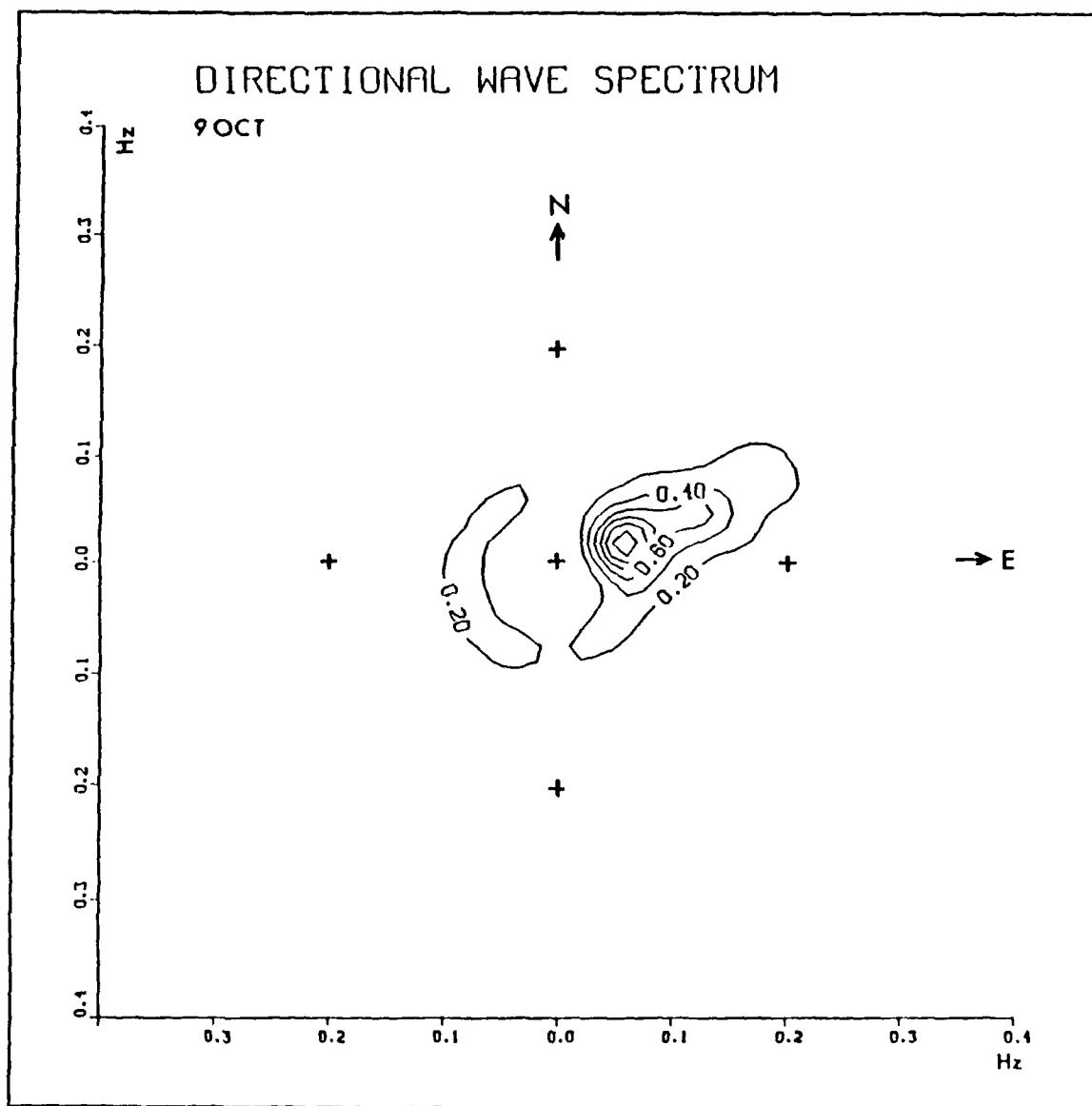


Figure 30. Directional wave spectrum for 9 October 6:40 to 7:40 computed by the Grauzinis method (top view): The energy spread over the west half plane has the largest value of the three one hour periods considered for short term analysis. Radial distance represents frequency and the plot is oriented north on top.

the component centered on the direction of the energy. The fraction of energy of the relocated uni-modal component will be minimal but of increasing value as the sharpness

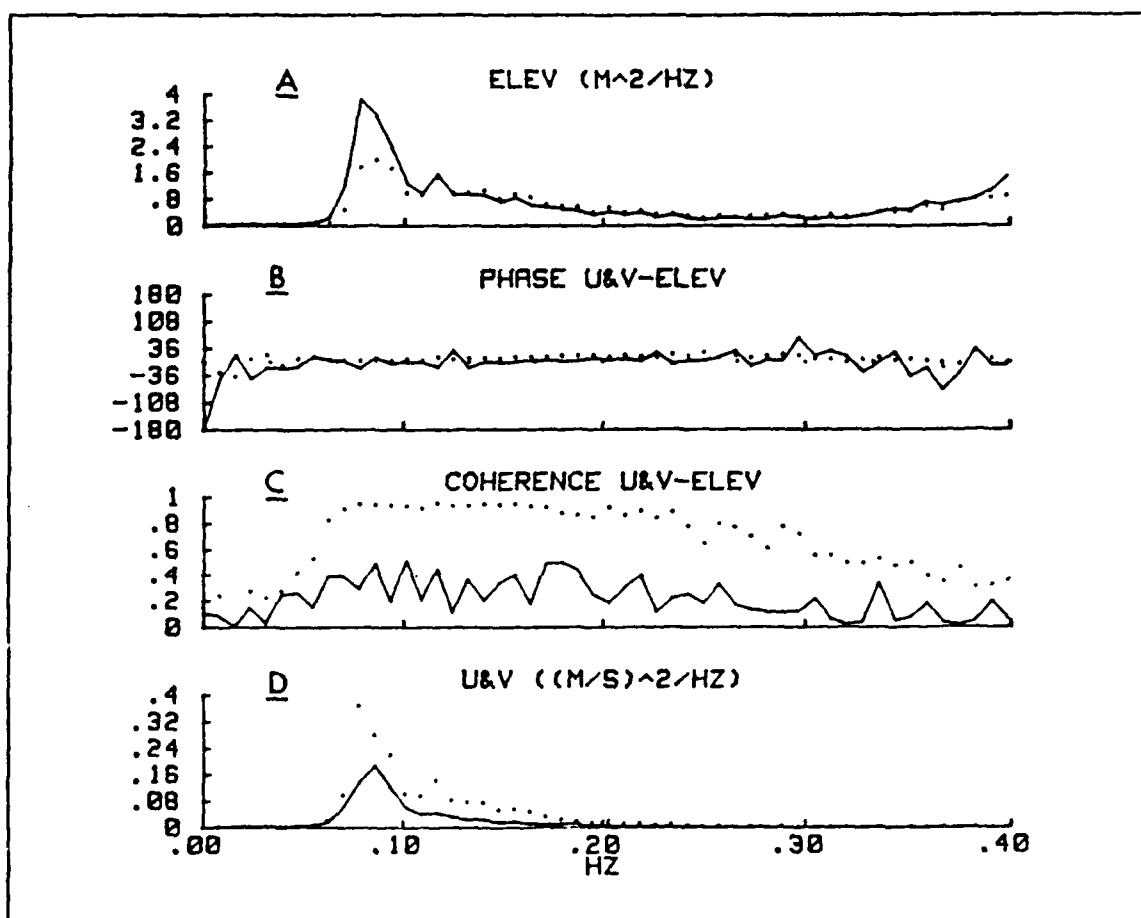


Figure 31. Spectral functions of the sea surface elevation and horizontal velocity components for 9 October 6:40 to 7:40: (A) Spectral density function of the sea surface elevation computed from the pressure data (solid line) and from the horizontal velocity (dotted line) do not compare as well as in the one hour periods of 6 and 8 October. (B) The phase spectra between the horizontal velocity components and the sea surface elevation verifies the in-phase relation predicted by the linear wave theory. (C) Coherence spectra between the horizontal velocity components and the sea surface elevation, shows a significant smaller value for the u component (solid line). (D) The spectral density of the two orthogonal components of the horizontal velocity (u solid line and v dotted line) shows different peaks for the two spectra, and more energy is associated with the v component.

of the model distribution decreases. This process is illustrated in Figure 32 for the period of 8 of October from 8:40 to 9:40. The directional spectra shown correspond to the wrapped-Cauchy (D2) and wrapped-normal (D3) model distributions, the first being considerably sharper. The amplitude of the annulus of energy for D4 is twice the amplitude for D2. This relocation of energy amounts to a decrease of the spectral value in the range of frequencies of significant energy. A reduction of the error introduced by this process can be accomplished by considering sharper model distributions. It is hypothesized that the energy contained in this annulus is an indicator of the best fitting model distribution. It should be noted that for the selected one hour periods, the beam separation index for the majority of the frequencies was smaller for the wrapped-Cauchy model distribution. The analysis of the results does not show a second annulus of energy that can be observed at the maximum frequency. This outer annulus of energy is not a consequence of the method used to compute directional spectrum. It represents the effects of noise, which is related to the approximation of the instantaneous pressure at the central point of the slope array, and to the computation of the sea surface elevation with the use of the transfer function given by linear wave theory, which amplifies noise strongly with increasing frequency. The significance of the results using the exact Fourier representation method must be interpreted recalling that only the Fourier coefficients through second order are matched, that at most bi-modal distributions of energy can be resolved and that there is a significant dependence of the results on the relative sharpness of the input and model distributions.

2. Coherence function

The results obtained for the coherence functions between the sea surface elevation and the two orthogonal components of the horizontal velocity verify the theoretical results. In the theoretical background, it was noted that the coherence function between the sea surface elevation and the horizontal components of the velocity depended on the bivariate wave spectrum. The results of the experiment show that the values of the coherence function are greater for the component that had the major contribution of the wave field, that is, the coherence function had greater values for the component that had the smaller turbulent to wave induced ratio assuming isotropy of the turbulent field. An attempt was made to compute the coherence function using the information given by the directional wave spectrum and the theoretical definition of the coherence function for statistically independent wave induced and turbulent components of the velocity, equations [82] and [83]. The estimate of the turbulence spectrum was obtained by linear filtration assuming isotropy of the turbulent field.

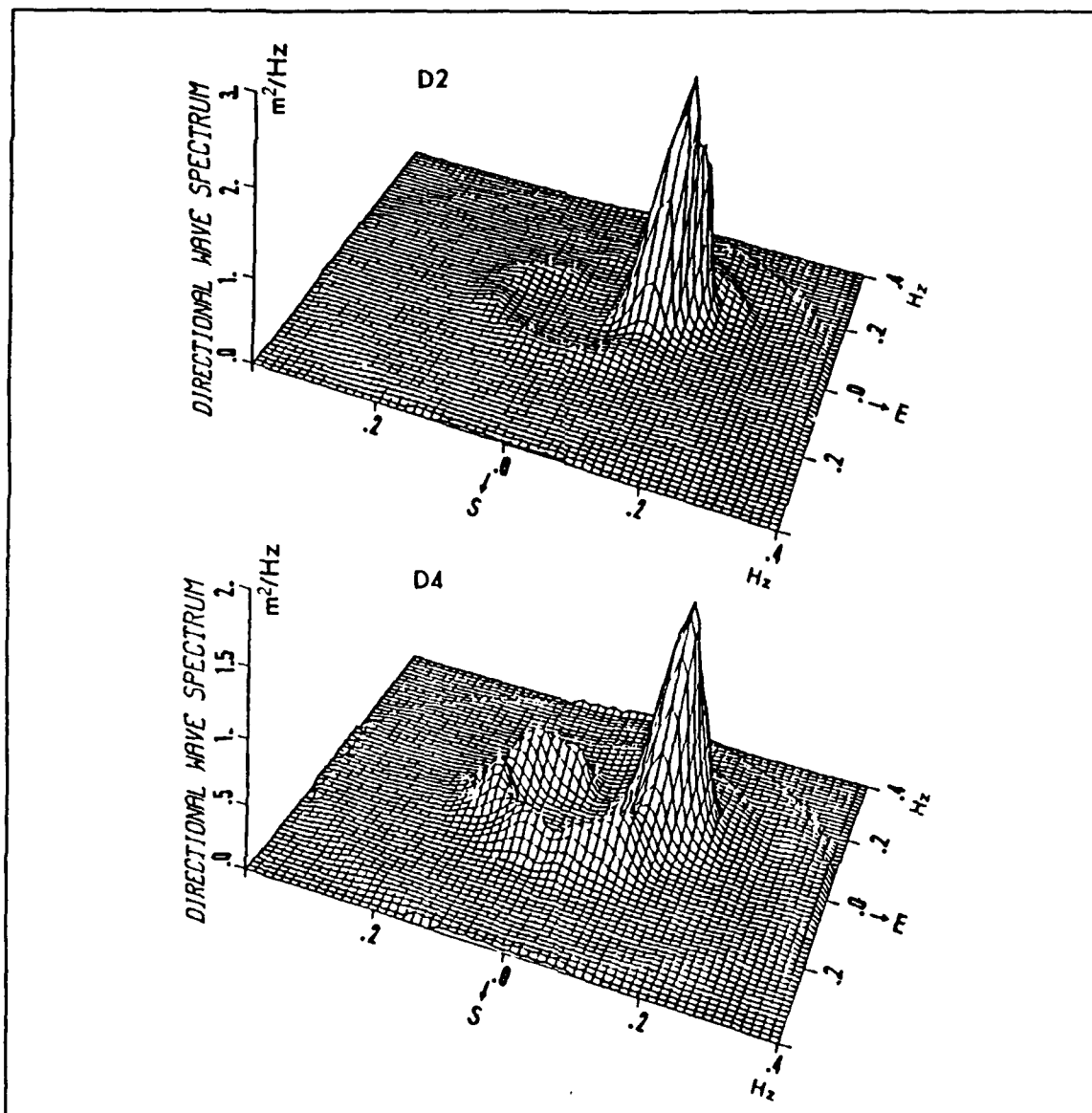


Figure 32. Directional spectrum computed by the Graüzinis method: The annulus of energy in the representative frequency band is considerably reduced for the sharper model distribution D2.

3. Phase spectrum

The computed phase spectra between the horizontal velocity components and the sea surface elevation were similar to the observations of Thornton and Kraphol (1974) and the results of linear wave theory. For the three one hour periods, the com-

ponents of the horizontal velocity and the sea surface elevation were in-phase, within the predicted phase shift due to the non-centered position of the electromagnetic current meter.

4. The spectrum of the sea surface elevation

The comparison of the spectra of the sea surface elevation from the measurements of pressure and from the horizontal velocities show good agreement for the three one hour periods analyzed. The results computed for 9 of October from the two data sets are not statistically different at the 95% confidence level. It must be noticed that the comparison of the two spectral density functions departs from the linear wave theory for both spectra. The direct observation of the sea surface elevation would introduce more meaning to the comparison and allow for a significant verification of the linear wave theory. The same can be said if the vertical component of the velocity field was available. The vertical component is not affected by directional effects as happens with the horizontal velocity components, and this effect has been shown to be related both to the wave and mean flow field.

V. CONCLUSIONS AND RECOMMENDATIONS

The new method of computing directional wave spectrum developed by Grauzinis (1989) verifies a necessary, but not sufficient, condition for the estimation of high resolution bivariate wave spectrum since only the Fourier coefficients through second order are matched. The ambiguity of the detailed shape of the directional wave spectrum is due to the lack of a strong indicator for the best model fitting distribution. The results obtained with this new method have given good indications of its capabilities. The possibility of resolving bi-modal energy distributions without a priori or a posteriori assumptions constitutes a significant improvement.

The velocity field measurements confirmed previous observations and theoretical results. Phase relations show a behavior as expected from linear wave theory. Coherence functions emphasized the directional effects of the wave field. Statistically equivalent results were obtained for the spectral density functions of the sea surface elevation computed from the pressure and horizontal velocity measurements using the transfer functions derived from the linear wave theory.

The instrumentation deployed during the SAXON experiment provided a fairly complete set of measurements. Improvements can be considered. The direct measurement of the sea surface elevation is of great importance, particularly at the central point of the frame of instruments. This measurement gives the possibility of computing higher order Fourier coefficients of the sea surface and improving the directional spectrum computation. When bistatic acoustic doppler profiler data are available, more significant tests of the spectral relations between measured quantities will be possible, and a far more detailed view of stress transfer and the turbulent field should be available.

The analysis of the experiment has shown a wide range of forcing conditions that will allow different kinematic responses of the upper ocean boundary layer to be studied. The availability of the three components of the velocity field throughout the water column will give a new meaning to the observations. A cross check of measurements and methods will be then possible, and a significative improvement on the understanding of the upper ocean boundary layer is expected.

The review of theoretical results has shown the necessity for new developments. The separation of the strong wave signal from the small background turbulence will provide

a continuing challenge. The study of the directional spreading effects of the wave field in the signal at depth also needs to be considered.

LIST OF REFERENCES

- Barber, N.F., 1946. Measurements of sea conditions by the motion of a floating buoy. *Admiralty Res. Lab. Report 103.40/n2/W*, Teddington.
- Bendat, J.S. and Piersol, A.L., 1986. *Random Data*. Wiley-Interscience, 566 pp.
- Bye, J.A.T., 1965. Wind driven circulation in unstratified lake. *Limnol. Oceanogr.*, 10, 451-458.
- Cartwright, D.E., 1963. Use of directional spectra in studying the output of a wave recorder on a moving ship. *Ocean wave spectra*, Prentice-Hall, Englewood Cliffs, N.J.
- Cavaleri, L. and S. Zechetto, 1987. Reynolds stresses under wind waves. *J. Geophys. Res.*, 92, 3894-3904.
- Churchill, J.H. and G.T. Csanady, 1983. Near-surface measurements of quasi-lagrangian velocities in open water. *J. Phys. Oceanogr.*, 13, 1669-1680.
- Cramer, H., 1962. *Random variables and probability*. 2nd ed., Cambridge University Press.
- Davis, R.E. and L.A. Regier, 1977. Methods for estimating directional wave spectrum from multi-element array. *J. Mar. Res.*, 35(3), 453-477.
- Ekman, V.W., 1905. *Ark Math. Astr. Och. Fys.* 2, No. 11.
- Grauzinis, V.J., 1989. *Personal communication*.
- Holton, J.R., 1979. *An introduction to dynamic meteorology*, 2nd ed., Academic Press, Inc., 391 pp.
- Kinsman, B., 1965. *Wind Waves*. Prentice-Hall, Englewood Cliffs, N.J., 676 pp.
- Longuet-Higgins, M.S., D.E. Cartwright and N.D. Smith, 1963. Observations of the directional spectrum of sea waves using the motions of a floating buoy. *Ocean wave spectra*, Prentice-Hall, Englewood Cliffs, N.J., 111-136.
- Lumley, J.L. and H.A. Panofsky, 1964. *The structure of atmospheric turbulence*, Wiley-Interscience.
- Munk, W.H., G.R. Miller, F.E. Snodgrass and N.F. Barber, 1963. Directional recording of swell from distant storms. *Phil. Trans., A*, 255, 505-584.
- Panofsky, H.A. and J.A. Dutton, 1984. *Atmospheric turbulence*, Wiley-Interscience, 397 pp.
- Phillips, O.M., 1977. *Dynamics of the upper ocean*. 2nd ed., Cambridge University Press, 261 pp.

- Prandtl, L., 1925. *Z. angew. Math. u. Mech.*, 5, 136.
- Richman, J.H., R.A. De Szoeke and R.E. Davis, 1987. Measurements of near-surface shear in the ocean. *J. Geophys. Res.*, 92, 2851-2858.
- Seitz, R.C., 1971. Measurements of a three dimensional field of water velocities at a depth of one meter in a estuary. *J. Mar. Res.*, 29, 140-150.
- Seymour, R.J. and A.L. Higgins, 1977. A slope array for estimating wave direction. *Nearshore sediment transport study workshop on instrumentation for nearshore processes*, Sea Grant pub.no. 62, 133-142.
- Shonting, D.H., 1970. Observations of the Reynolds stresses in wind waves. *Pure Appl. Geophys.*, 81/4, 202-210.
- Thornton, E.B. and R.F. Kraphol, 1974. Water particles velocities measured under ocean waves. *J. Geophys. Res.*, 79, 847-852.
- Wu, J., 1975. Wind induced drift currents. *J. Fluid Mech.*, 68, 49-70.
- Yefimov, V.V. and G.N. Khristoforov, 1971. Spectra and statistical relations between the velocity fluctuations in the upper layer of the sea and surface waves. *Atmos. Oceanic Phys.*, 7(12), 1290-1310.

INITIAL DISTRIBUTION LIST

		No. Copies
1.	Defense Technical Information Center Cameron Station Alexandria, VA 22304-6145	2
2.	Library, Code 0142 Naval Postgraduate School Monterey, CA 93943-5002	2
3.	Chairman (Code 68Co) Department of Oceanography Naval Postgraduate School Monterey, CA 93943	1
4.	Chairman (Code 63Rd) Department of Meteorology Naval Postgraduate School Monterey, CA 93943	1
3.	Dr. E.B. Thornton (Code 68TM) Department of Oceanography Naval Postgraduate School Monterey, CA 93943	3
5.	Mr. T P. Stanton (Code 68ST) Department of Oceanography Naval Postgraduate School Monterey, CA 93943	2
6.	Director, Naval Oceanography Division Naval Observatory 34th and Massachusetts Avenue NW Washington, DC 20390	1
7.	Commanding Officer Fleet Numerical Oceanography Center Monterey, CA 93943	1
8.	Commanding Officer Naval Environmental Prediction Research Facility Monterey, CA 93943	1
9.	Naval Ocean Research and Development Activity NSTL Station Bay St. Louis, MS 39522	1

- | | | |
|-----|---|---|
| 10. | Naval Oceanographic Office
Stennis Space Center
Bay St. Louis, MS 39522 | 1 |
| 11. | Office of Naval Research (Code 420)
800 N. Quincy Street
Arlington, VA 22217 | 1 |
| 12. | Direccao do Servico de Instrucao e Treino
Marinha Portuguesa
Rua do Arsenal
1100 Lisboa
Portugal | 1 |
| 13. | Director Geral do Instituto Hidrografico
Instituto Hidrografico
Rua das Trinas, 49
1200 Lisboa
Portugal | 2 |
| 14. | LT Manuel A. F. Pinto de Abreu
Department of Oceanography
Naval Postgraduate School
Monterey, CA 93943 | 4 |
| 15. | LCDR Carlos N. Lopes da Costa
Instituto Hidrografico
Rua das Trinas, 49
1200 Lisboa
Portugal | 1 |
| 16. | Mr. V.J. Grauzinis
Transpectrum Corporation
2011 Cecilia Terrace
San Diego, CA 92110 | 1 |
| 17. | Director of Research Administration (Code 012)
Naval Postgraduate School
Monterey, CA 93943 | 1 |